Architecture of a minimal signaling pathway explains the T-cell response to a 1 million-fold variation in antigen affinity and dose

Melissa Lever[a,1], Hong-Sheng Lim[a,1], Philipp Kruger[a,1], John Nguyen[a], Nicola Trendel[a], Enas Abu-Shah[a], Philip Kumar Maini[b], Philip Anton van der Merwe[a], and Omer Dushek[a,b,2]

[a]Sir William Dunn School of Pathology, University of Oxford, Oxford OX1 3RE, United Kingdom; and [b]Wolfson Centre for Mathematical Biology, Mathematical Institute, University of Oxford, Oxford OX2 6GG, United Kingdom

Edited by K. Christopher Garcia, Stanford University, Stanford, CA, and approved August 26, 2016 (received for review June 2, 2016)

T cells must respond differently to antigens of varying affinity presented at different doses. Previous attempts to map peptide MHC (pMHC) affinity onto T-cell responses have produced inconsistent patterns of responses, preventing formulations of canonical models of T-cell signaling. Here, a systematic analysis of T-cell responses to 1 million-fold variations in both pMHC affinity and dose produced bell-shaped dose–response curves and different optimal pMHC affinities at different pMHC doses. Using sequential model rejection/identification algorithms, we identified a unique, minimal model of cellular signaling incorporating kinetic proofreading with limited signaling coupled to an incoherent feed-forward loop (KPL-IFF) that reproduces these observations. We show that the KPL-IFF model correctly predicts the T-cell response to antigen copresentation. Our work offers a general approach for studying cellular signaling that does not require full details of biochemical pathways.

T-cell receptor | signaling | pathway architecture | immunology | systems biology

T-cell activation is critical for initiating and regulating adaptive immunity (1). It proceeds when T-cell receptors (TCRs) on the T-cell surface bind to antigenic peptides loaded on major histocompatibility complexes (pMHCs). Binding of pMHC ligands to the TCR initiates a large signal transduction cascade that can lead to T-cell activation as measured by functional responses such as proliferation, differentiation, target cell killing, and the production and secretion of effector cytokines. These responses critically depend on the pMHC affinity and dose. T cells are known to discriminate between normal and infected or cancerous cells based on differences in pMHC affinity (2, 3). It is also appreciated that the pMHC dose determines, for example, the peripheral induction of regulatory T cells (4, 5). Although the proteins that form the TCR-regulated signaling network have been identified (6, 7), it remains unclear how the architecture they form integrates the pMHC affinity and dose into T-cell activation (8, 9).

Studies performed over the last two decades have focused on empirically mapping the relationship between pMHC affinity and T-cell activation (5, 10–24). A number of studies have reported an optimal pMHC affinity for T-cell activation, but other studies have failed to observe the optimum. Interestingly, a subset of studies have suggested that the optimal pMHC affinity may be less pronounced at high pMHC doses (13, 22). The mechanism underlying an optimal pMHC affinity (or half-life) is proposed to be a trade-off between serial binding and kinetic proofreading, but we have recently shown that this trade-off would lead to an optimal pMHC affinity at all pMHC doses (9).

An accurate model of T-cell signaling pathways that can predict the T-cell response to a broad range of antigen ligand affinity and dose is important not only to understand physiological T-cell responses but also in the rational design of T-cell–based therapies (25). Engineered therapeutic TCRs and chimeric antigen receptors (CARs) have been produced to bind, for example, cancer antigens with high affinity (dissociation constants, K_d, in the picomolar to nanomolar range). A specific example is the NY-ESO-1 cancer antigen, for which both high-affinity TCRs and CARs have been produced (26, 27). The optimizing of these therapies has focused, in part, on trying to determine the optimal receptor affinity for clinical efficacy (20, 22, 28–30; reviewed in ref. 31).

A key challenge in the study of cellular signaling in general, and particularly in T cells, is the organization of large amounts of molecular information into accurate mathematical models that can predict cellular responses (32). The reductionist approach has been to incorporate the known biochemistry into mathematical models, but it is well recognized that this relies on many assumptions (e.g., which proteins and interactions to include, their binding and reaction rate constants, concentrations, etc.) leading to models whose accuracy is difficult to determine (32, 33). This may, in part, explain why canonical models of T-cell signaling have been elusive (Fig. 1*A*). An alternative holistic approach is to infer models from experimental data without any prior assumptions (34–39) (e.g., of the known biochemistry).

In this work, we used the high-affinity engineered c58c61 TCR that binds the NY-ESO-1 cancer antigen (27) to measure primary human T-cell activation in response to a 1 million-fold variation in pMHC affinity and dose. We found bell-shaped dose–response curves with inhibition at high pMHC doses. Moreover, different pMHCs (and hence different affinities) produced the largest T-cell response at different pMHC doses. Without making prior assumptions about the known biochemistry, we identified a

Significance

T cells initiate and regulate adaptive immune responses when their T-cell antigen receptors recognize antigens. The T-cell response is known to depend on the antigen affinity/dose, but the precise relationship, and the mechanisms underlying it, are debated. To resolve the debate, we stimulated T cells with antigens spanning a 1 million-fold range in affinity/dose. We found that a different antigen (and hence different affinity) produced the largest T-cell response at different doses. Using model identification algorithms, we report a simple mechanistic model that can predict the T-cell response from the physiological low-affinity regime into the high-affinity regime applicable to therapeutic receptors.

Author contributions: M.L., H.-S.L., P.K., P.K.M., P.A.v.d.M., and O.D. designed research; M.L., H.-S.L., P.K., J.N., N.T., E.A.-S., and O.D. performed research; M.L., H.-S.L., P.K., J.N., N.T., E.A.-S., and O.D. contributed new reagents/analytic tools; M.L., H.-S.L., P.K., J.N., N.T., E.A.-S., P.K.M., P.A.v.d.M., and O.D. analyzed data; and M.L., H.-S.L., P.K., P.K.M., P.A.v.d.M., and O.D. wrote the paper.

The authors declare no conflict of interest.

This article is a PNAS Direct Submission.

[1]M.L., H.-S.L., and P.K. contributed equally to this work.

[2]To whom correspondence should be addressed. Email: omer.dushek@path.ox.ac.uk.

This article contains supporting information online at www.pnas.org/lookup/suppl/doi:10.1073/pnas.1608820113/-/DCSupplemental.

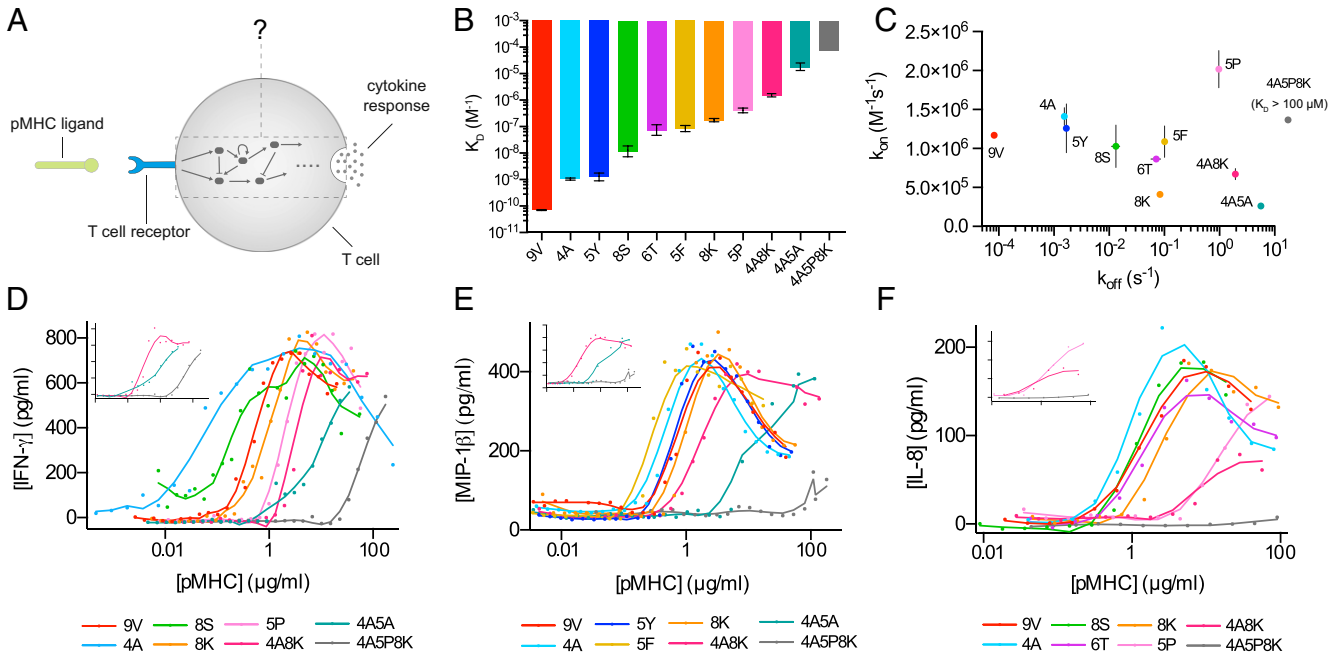

Fig. 1. T-cell activation in response to a 1 million-fold variation in pMHC affinity and dose. (*A*) Schematic illustrating that the signaling architecture linking the TCR to cytokine production is unknown. (*B*) Affinities (displayed as dissociation constants, K_d) and (*C*) kinetics of the c58c61 TCR interacting with 11 pMHC ligands determined using surface plasmon resonance (see also *SI Appendix*, Fig. S1 and Table S1). T-cell activation as measured by supernatant (*D*) IFN-γ and (*E*) MIP-1β in primary T cells after 4 h and (*F*) IL-8 in Jurkat T cells after 16 h transduced with the c58c61 TCR (insets show the three lowest-affinity ligands in each experiment). Ligand color scheme is identical across all panels. Additional data, including additional concentrations, additional ligands, pMHC immobilization controls, and TCR expression levels, are summarized in *SI Appendix*, Fig. S2.

unique and modular pathway architecture for cellular signaling that reproduced these observations: kinetic proofreading with limited signaling coupled to an incoherent feed-forward motif (KPL-IFF). We show that the identified KPL-IFF model predicts the outcome of pMHC copresentation experiments. These mechanistic insights force a revision of the serial binding and kinetic proofreading model for T-cell activation. The revised KPL-IFF model now predicts T-cell activation from the physiological low-affinity regime into the high-affinity regime applicable to therapeutic TCRs and CARs.

Results

T-Cell Activation in Response to a 1 Million-Fold Variation in Antigen Affinity/Dose. As a first step to identify a T-cell signaling model (Fig. 1*A*) we established a TCR/pMHC system with a large range of affinities by using the therapeutic affinity-matured c58c61 TCR that recognizes a peptide derived from the cancer antigen NY-ESO-1 in complex with HLA-A*02:01 (K_d ~ 50 pM) (27). This TCR contains 14 amino acid substitutions (primarily at the contact interface) but maintains the same binding mode as the parental 1G4 TCR (40). Using single, double, and triple peptide mutations we produced a panel of 11 pMHCs that span a 1 million-fold range in affinity (Fig. 1 *B* and *C* and *SI Appendix*, Table S1 and Fig. S1). The observed changes in affinity were largely a result of changes in the off-rate k_{off}.

We next transduced the c58c61 TCR into primary human $CD8^+$ T cells and the Jurkat T-cell line (*SI Appendix*, Fig. S2*A*) before stimulating them with a 1 million-fold range of pMHC concentration. In the case of the primary T cells we measured the supernatant concentration of IFN-γ or macrophage inflammatory protein 1-β (MIP-1β) after 4 h of stimulation (Fig. 1 *D* and *E* and *SI Appendix*, Fig. S2*B*). In the case of the Jurkat T cells we measured the supernatant concentration of IL-8 after 16 h (Fig. 1*F* and *SI Appendix*, Fig. S2*C*) or the transcriptional activity of activator protein 1 (AP-1) and nuclear factor of activated T cells (NFAT) (*SI Appendix*, Fig. S2*D*).

Four striking features were observed. First, the dose–response seemed to exhibit a bell shape with reduced cytokine production at high pMHC concentrations. This bell shape was less pronounced or absent for low-affinity ligands, which is consistent with published studies reporting a sigmoidal dose–response for low-affinity ligands (14, 15, 17, 18, 21, 23, 41). Second, the peak amplitude of the bell-shaped dose–response was similar for pMHCs despite large differences in their affinities. The next two features describe the observation that the pMHC that produced the most cytokine was dose-dependent. At higher concentrations (to the right of the peaks) there is an obvious intersection of the dose–response curves so that different pMHC ligands produce the most cytokine at different doses (e.g., 4A8K or 4A5A in Fig. 1 *D*–*F*). In contrast, at lower concentrations (to the left of the peaks) curve intersection is not apparent, so that a single intermediate affinity pMHC produces the most cytokine.

These four phenotypic features are summarized as follows:

i) Bell-shaped dose-response for high- but not low-affinity ligands.
ii) Peak amplitude of bell-shaped dose-response is independent of affinity.
iii) A single intermediate affinity ligand produces largest response at low doses (left of the peak).
iv) Different intermediate affinity ligands produce the largest response at high doses (right of the peak).

Although a bell-shaped dose–response can be a result of activation-induced cell death (42), this is unlikely to be the case here. We found that the dose–response for cytokine production appeared bell-shaped at all times with continued cytokine production to the right of the peak (Fig. 2*A*). Moreover, direct detection of apoptosis by annexin V binding revealed a maximum of only 10%, which is insufficient to explain the observed reduction in cytokine production (Fig. 2*B*). Further, lower levels of cytokine observed to the right of the peak were associated with lower levels of annexin V, which is inconsistent with the hypothesis that lower cytokine is a

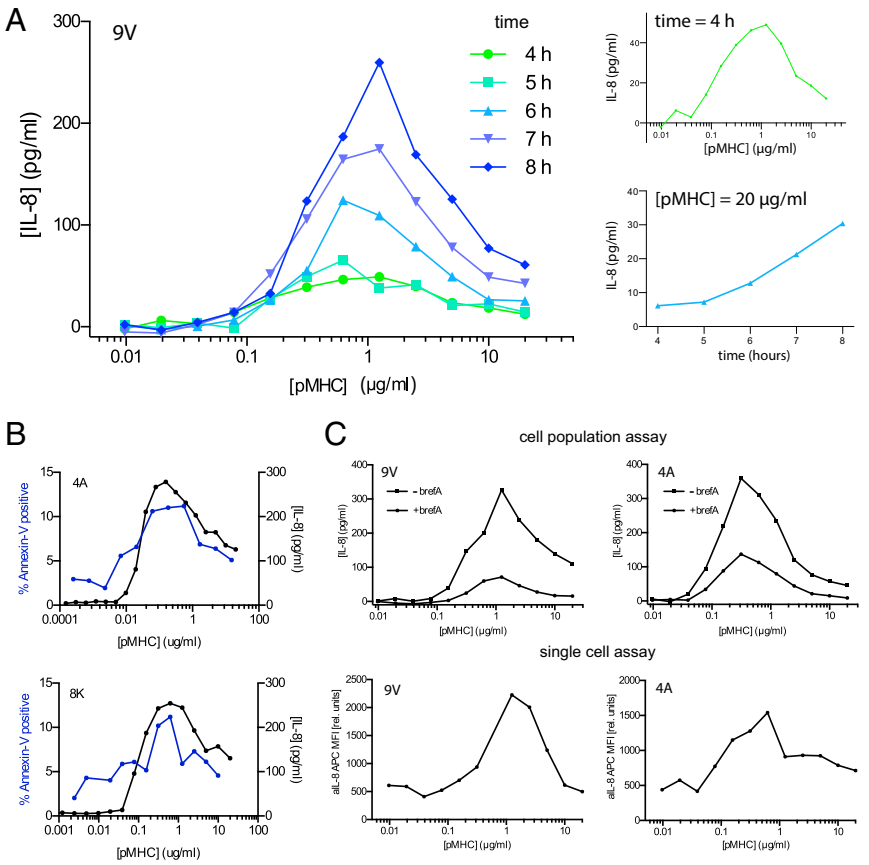

Fig. 2. A bell-shaped dose–response is a consequence of reduced cytokine production at high pMHC concentrations. (*A*) T-cell activation dose–response curves at the indicated time points (*Left*) highlighting the bell-shape at early times (4 h) and continued cytokine production at the largest pMHC concentration (*Right*, *Top* and *Bottom*). (*B*) Percent of T cells positive for annexin V (blue, left axis) determined at the end of a 16-h functional assay where the supernatant concentration of IL-8 was also determined (black, right axis). (*C*) Comparison of supernatant IL-8 production at the population level (*Top*) with the corresponding single cell IL-8 production by flow cytometry (*Bottom*) at 16 h. Brefeldin A was added to block cytokine secretion for the last 3 h of the assay (reducing supernatant cytokine in the cell population assay). Jurkat T cells are used to generate all panels with the indicated pMHC ligands. See *SI Appendix*, Fig. S2*E* for single-cell cytokine production in primary $CD8^+$ T cells.

result of increased apoptosis at high pMHC doses. These observations suggested a reduced rate of cytokine production per cell at high pMHC doses, which we confirmed using single-cell cytokine production in Jurkat T cells (Fig. 2*C*) and in primary T cells (*SI Appendix*, Fig. S2*E*).

We observed interdonor variability that could not be explained by differential TCR expression or pMHC activity. For example, the pMHC that produced the largest response to the left of the peak varied between 4A, 5Y, and 8S (compare Fig. 1*D* and *SI Appendix*, Fig. S2*B*). However, the feature that a single pMHC of intermediate affinity produced the largest response to the left of the peak was consistent. Therefore, although the quantitative features of the data exhibited variability, we observed a high level of consistency for the key qualitative phenotypic features. Similarly, we found that Jurkat T cells required a higher amount of antigen to produce cytokine but that the overall response exhibited the same qualitative phenotypic features observed in the primary T cells. Although these Jurkat T cells express CD8α, their reduced sensitivity may be related to the absence of CD8β, which has previously been shown to increase antigen sensitivity (12).

Sequential Model Rejection Identifies the KPL-IFF Model as Sufficient to Explain T-Cell Responses. We next identified a T-cell signaling network consistent with all key features by sequentially rejecting models. To do this, we tested models of increasing complexity starting with the simplest possible cellular mechanism, namely the occupancy model, which reduces cellular signaling to a single reaction (Fig. 3*A*). In this model, the pMHC ligand binds to the TCR to form a complex that directly activates a node *P* that is assumed to be linearly proportional to cytokine production. By examining the predicted dose–response curve for this model it is clear that the model is insufficient to explain the phenotypic features (e.g., it does not produce a bell-shaped dose–response, feature 1) and therefore we reject this model as a plausible model of T-cell signaling.

Bell-shaped dose–response curves can be produced by incoherent feed-forward motifs (Fig. 3*B*), which are common architectures in transcriptional networks (43). In this model, the TCR–pMHC complex directly inhibits *P* and indirectly activates *P* (by activating *Y*, which itself is able to activate *P*). The model can produce inhibition at high pMHC concentrations if the activatory pathway (through *Y*) saturates, allowing inhibition to dominate at the highest pMHC concentrations. The appearance of the bell shape in this model can explain the observation that a different pMHC affinity produces the largest response to the right of the peak (feature 4). However, this model is also rejected because it produces a bell-shaped dose–response for all pMHC ligands independent of their affinity (feature 1).

Bell-shaped dose–response curves can be produced for high- but not low-affinity ligands by introducing kinetic proofreading (Fig. 3*C*). In this model, the pMHC ligand does not trigger signaling immediately upon binding TCR but instead must remain bound until it becomes signaling-competent (denoted as C_1).

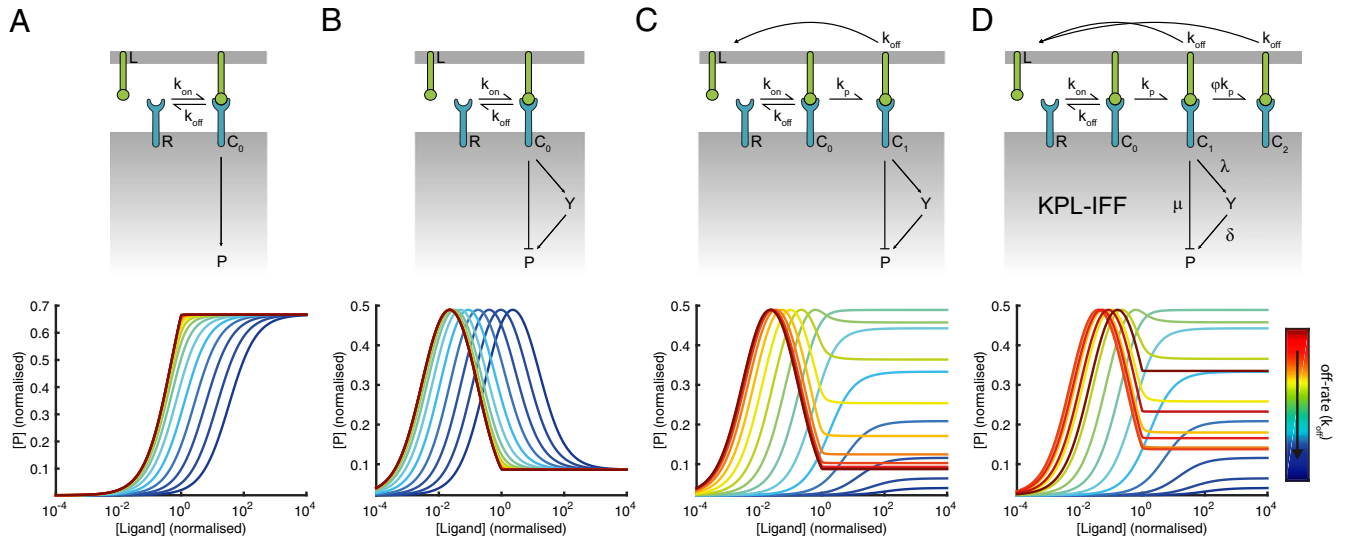

Fig. 3. Sequential model rejection reveals that kinetic proofreading with limited signaling coupled to an incoherent feed-forward loop can produce all phenotypic features. The models considered, in order of increasing complexity, are (*A*) occupancy, (*B*) occupancy coupled to incoherent feed-forward, (*C*) kinetic proofreading coupled to incoherent feed-forward, and (*D*) KPL-IFF. All models include the reversible (serial) binding of pMHC ligands (L) to the TCR (R) to form complexes that can regulate the activation of a protein P that is taken to be a measure of T-cell activation. See *SI Appendix* for computational details and *SI Appendix*, Applet S1 for a tool that can be used to explore how the five parameters in the KPL-IFF model (k_p, ϕ, μ, λ, and δ) modulate the predicted dose–response for antigens of different affinities.

This delay means that low-affinity pMHCs (with faster k_{off}) induce a lower maximal concentration of C_1 than high-affinity pMHC (see *SI Appendix*, Fig. S3 for a plot of C_1 for pMHC with different values of k_{off}). If this is below the level at which Y saturates then inhibition at high pMHC concentrations will not be observed with low-affinity pMHC. As expected, kinetic proofreading has improved antigen discrimination by dramatically decreasing the T-cell response to low-affinity pMHC. This model, however, is also rejected because it predicts that the highest-affinity ligand will produce the largest response left of the peak in contrast to experimental observations (feature 3).

Introducing limited signaling into kinetic proofreading can produce an optimal affinity over a range of pMHC concentrations (9) (Fig. 3*D*). In this model, activated TCR–pMHC complexes (C_1) signal for a limited period before converting to a nonsignaling state (C_2), thereby introducing a penalty for pMHCs that remain bound for long periods of time. This model is now able to explain all key features and we therefore accept the KPL-IFF model as a plausible signaling model for T-cell activation.

Systematic Model Identification Confirms That the KPL-IFF Model Is Unique. Having identified the KPL-IFF model as sufficient to explain all phenotypic features, we next determined whether other models, with a potentially different underlying mechanism, can also explain all phenotypic features.

We first systematically examined models of equal or lower complexity compared to the KPL-IFF model. To do this, we studied all combinations of three reaction arrows between Y and P and the three receptor states (Fig. 4*A*). Of the 560 possible reaction networks (16 choose 3) only the 304 networks that contain a connection between the ligand and P were analyzed. For each of these putative signaling networks, we performed an exhaustive search that included a dense parameter scan followed by optimization of the five free parameters (*SI Appendix*, Fig. S4). The output of the analysis is a list of networks ordered by their ability to reproduce the phenotypic features (Movie S1). As expected, the first network to appear is the KPL-IFF model but, unexpectedly, the 303 subsequent networks were all unable to explain all phenotypic features.

We highlight three models from the network search that are inconsistent with the phenotypic features (Fig. 4 *B*–*D*). A mirrored model in which activation is direct but inhibition is indirect cannot produce a bell-shaped dose–response (feature 1) because activation cannot saturate (Fig. 4*B*). A redirected model where inhibition comes from an earlier complex not subjected to kinetic proofreading (Fig. 4*C*) cannot explain a different optimal pMHC affinity to the right of the peak (feature 4) or the observation that the peak response is similar for different affinity ligands (feature 2). Finally, models without an incoherent feed-forward loop but with negative feedback, although able to produce oscillations of P in time, cannot produce a bell-shaped dose–response (Fig. 4*D* and *SI Appendix*, Fig. S5; see also *SI Appendix* for a mathematical proof).

To determine whether more complex models can explain all key features using different mechanisms, we performed the same systematic network analysis on models with four reaction arrows between Y, P, and an additional node X and four receptor states (Fig. 4*E*). A systematic analysis of the 26,069 networks with a connection between the ligand and P revealed 274 compatible networks (*SI Appendix*, Movie S2). However, examining these 274 networks showed that the basic mechanism underlying all compatible networks was KPL-IFF. For example, the incoherent feed-forward loop could involve indirect inhibition so long as inhibition saturates after activation as a function of ligand dose (Fig. 4*F*) or it could involve both direct activation and inhibition with the net effect being inhibition (Fig. 4*G*). As above, negative feedback could not produce bell-shaped dose–response curves (Fig. 4*H*).

In summary, the KPL-IFF signaling network (Fig. 3*D*) is sufficient to explain all phenotypic features. Given that the systematic analyses implicitly include simpler models (e.g., by allowing for the magnitude of reaction arrows to be negligible) we were able to further conclude that the KPL-IFF model is the simplest model able to explain all features.

The KPL-IFF model contains five parameters: kinetic proofreading (k_p), limited signaling (ϕ), inhibition (μ), activation (δ), and amplification (λ). We used approximate Bayesian computations with sequential Monte Carlo to establish the set of these parameters that are able to reproduce the key features (44). We found that large variations of the parameters were possible provided that they

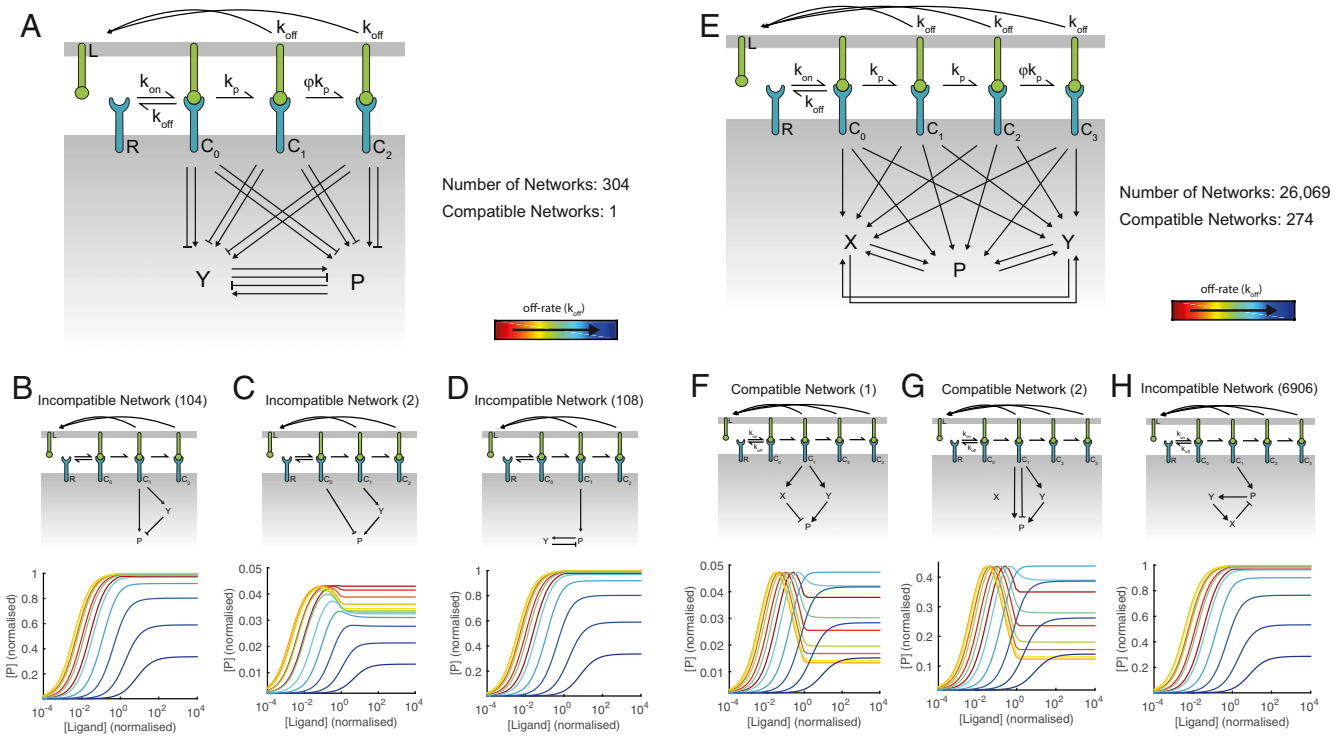

Fig. 4. Systematic analyses of signaling models reveals that the KPL-IFF mechanism is unique. (*A*) To determine whether other models of equal (or lower) complexity to the KPL-IFF model (Fig. 3*D*) are able to produce all phenotypic features we performed a systematic search of 304 network architectures with three reaction arrows between the receptor states (C_0, C_1, and C_2), *Y*, and *P*. The only network architecture that is able to produce all phenotypic features is the KPL-IFF model (Movie S1). Conversely, (*B*) the mirrored KPL-IFF, (*C*) the redirected KPL-IFF, and (*D*) negative feedback network architectures are unable to produce the phenotypic features. (*E*) To determine whether more complex models can reproduce the phenotypic features using mechanisms different from those invoked in the KPL-IFF model, we performed a systematic analysis of 26,069 network architectures with four reaction arrows between four receptor states and *Y*, *P*, and an additional node *X*. Both activation and inhibition are considered but for clarity only activation arrows are depicted. We found 274 networks compatible with all phenotypic features but all of these networks relied on the KPL-IFF mechanism (*SI Appendix*, Movie S2). (*F* and *G*) Two representative compatible networks show that although the network is more complicated both rely on the KPL-IFF mechanism. (*H*) As before, negative feedback in the absence of incoherent feed-forward is unable to produce the phenotypic features. See *SI Appendix* for computational details.

obeyed certain relationships (*SI Appendix*, Fig. S6). For example, we found that μ and δ can vary by 1,000-fold provided that $\mu > \delta$ and that increases in ϕ can reproduce the phenotypic features provided that k_p decreased proportionally. Using the provided applet (*SI Appendix*), we find that bell-shaped dose–response curves are less pronounced when the condition $\mu > \delta$ is not satisfied. A large variation in the parameters is tolerated because the phenotypic features are scale-free (*SI Appendix*).

The KPL-IFF Model Predicts the T-Cell Response to Copresentation of pMHC Ligands. T cells generally experience mixtures of pMHC ligands when becoming activated. Previous studies have shown that copresentation of an additional pMHC can modulate the T-cell response in various ways, including both enhancing and inhibiting T-cell activation (45).

To address the effects of pMHC copresentation, we extended the KPL-IFF model to include an additional pMHC ligand with different binding kinetics and concentrations (Fig. 5*A*). We used the extended KPL-IFF model to predict the T-cell response to a titration of a lower-affinity ligand in the presence of fixed concentrations of a higher-affinity ligand (Fig. 5*B*). As a result of the incoherent feed-forward loop the model predicted a sigmoidal dose–response when the concentration of the high-affinity ligand was left of its peak ($\lesssim 0.025$) and a constant response when the concentration of the high-affinity ligand was right of its peak ($\gtrsim 0.025$). This is a direct result of the saturating activating pathway of the incoherent feed-forward. Surprisingly, the model predicted that T-cell activation cannot be inhibited by signals induced by the low-affinity ligand even when the high-affinity ligand is presented at concentrations that saturate the activation pathway of the incoherent feed-forward. We confirmed these predictions by stimulating T cells with a titration of the lower-affinity ligand, 5P, in the presence of fixed concentrations of the higher-affinity ligand, 4A (Fig. 5*C*). As predicted by the model, the dose–response curves appeared sigmoidal at lower doses of 4A and largely constant at higher doses, without any obvious inhibition of T-cell activation by 5P.

Discussion

We have measured the T-cell response to a 1 million-fold variation in antigen affinity and dose. We found bell-shaped dose–response curves with a different pMHC (and hence different affinity) producing the largest T-cell response at different doses. We show, without making prior biochemical assumptions and with the constraint of parsimony, that the KPL-IFF architecture is the only model identified able to explain all phenotypic features of the experimental data. We further confirmed predictions of the model concerning pMHC copresentation. Remarkably, the KPL-IFF model can explain the T-cell response to a 1 million-fold variation in antigen affinity and dose based on a simple pathway architecture despite the enormous molecular complexity in T-cell signaling.

The present work has uncovered two independent mechanisms that lead to an optimal pMHC affinity. At low doses (left of the peak) we find that limited signaling through the TCR allows a single intermediate affinity pMHC to dominate the dose–response curve, whereas at higher doses (right of the peak) a different pMHC affinity produces the most cytokine as a result of the bell-shaped dose–response curves

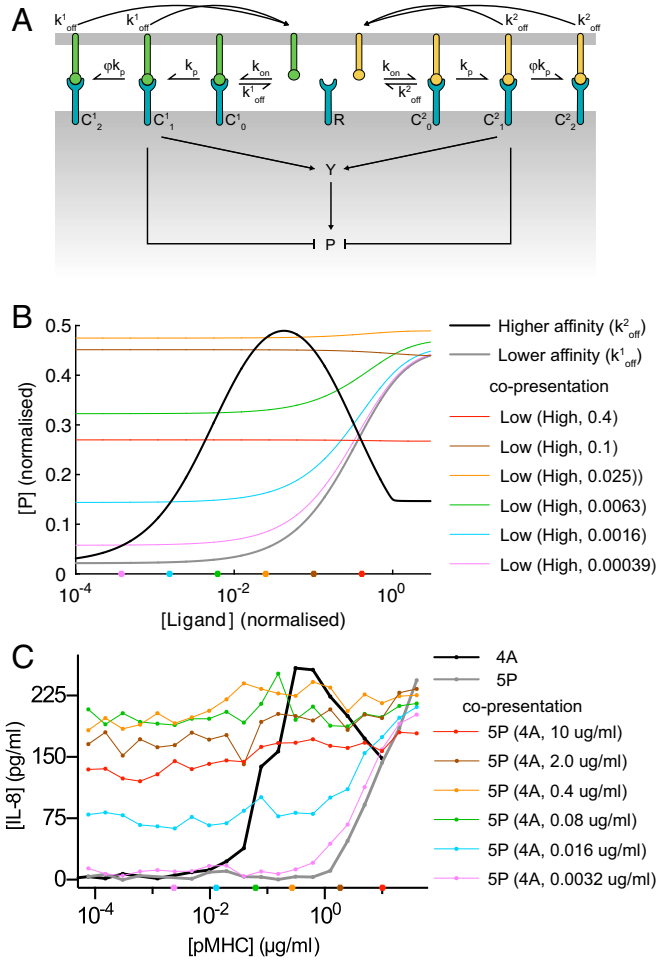

Fig. 5. The KPL-IFF model predicts T-cell activation in response to copresentation of pMHC ligands. (*A*) Schematic of signal integration by two distinct populations of pMHC ligands in the context of the KPL-IFF model. (*B*) The model predicts that a titration of a low-affinity ligand ($k^1_{off} = 1\ s^{-1}$) in the presence of a fixed concentration of a high-affinity ligand ($k^2_{off} = 0.001\ s^{-1}$) will be either sigmoidal or constant when the concentration of the high-affinity ligand is left of its peak (purple, cyan, and green) or right of its peak (orange, brown, and red), respectively. Appreciable inhibition by the low-affinity ligand is not predicted even when the activating pathway has saturated. (*C*) T-cell activation as measured by supernatant IL-8 released by Jurkat T cells in response to a titration of 5P (lower-affinity ligand) at the indicated fixed concentrations of 4A (higher-affinity ligand). The fixed concentration of the higher-affinity ligand is indicated and labeled on the *x* axis as colored circles. Data are representative of two independent experiments. See *SI Appendix* for computational details.

produced by the incoherent feed-forward loop. In light of our comprehensive data, it is likely that discrepancies between previous studies were a result of a limited range of tested pMHC affinity and dose. The model may account for previous work showing a bell-shaped dose–response in the induction of regulatory T cells (5).

Modified TCRs and CARs often target tumor-associated antigens that are differentially expressed between normal and cancer cells. Therefore, the antigen dose can be a critical determinant of successful immunotherapy. As a result of the bell-shaped dose–response, we find that low-affinity receptors can actually outperform high-affinity receptors at high antigen doses. Our model provides a rationale for optimizing the affinity of therapeutic receptors based on the target antigen dose, as recently proposed for a CAR (30). We provide a tool that can be used to examine the predicted T-cell response for antigens of different affinities presented at different doses (*SI Appendix*, Applet S1).

A number of studies have implicated negative feedback in TCR signaling (6), but we find that negative feedback cannot explain the phenotypic features of T-cell activation. For example, negative feedback cannot produce bell-shaped dose–response curves. We note that our model does not preclude the existence of signaling proteins with negative effects, such as tyrosine phosphatases that can determine, for example, the net rate of TCR phosphorylation (k_p). Negative feedback may be more important for the short-timescale process of antigen discrimination rather than the longer timescale process of T-cell activation that has been the focus of the present study (1, 6).

The limited signaling mechanism is related to previous work showing that a trade-off between serial binding and kinetic proofreading leads to an optimal pMHC half-life (10, 46). Serial binding of a single pMHC to many TCRs can increase signaling when the pMHC concentration is low and individual TCRs signal for a limited period upon binding. Under these conditions longer binding half-lives can reduce the number of productive TCR engagements (9). We find that at low doses reduced signaling is only observed when the TCR/pMHC half-life measured in solution is longer than 1 min (e.g., low dose of 4A, 5Y, and 8S compared with 9V in *SI Appendix*, Fig. S2 *B* and *C*). It follows that although limited signaling (and hence serial binding) may not be critical for physiological TCR-pMHC interactions, which have half-lives that last seconds, it is likely to be important for the design of high-affinity therapeutic TCRs or CARs for T-cell adoptive transfer therapies (25).

The internalization of TCR is known to take place upon TCR triggering (1, 46) and it can be realized by different mechanisms. Intracellular signaling induced by activated TCR that leads to TCR internalization is a form of negative feedback and, as discussed above, negative feedback cannot explain the observed phenotypic features. Limited signaling may result from the tagging of TCR for internalization and explicitly including this internalization, without incoherent feed-forward, does not lead to bell-shaped dose–response curves in the steady state (*SI Appendix*, Fig. S8). The KPL-IFF model may implicitly be capturing TCR surface dynamics because directed movement (47) combined with polarized recycling (48, 49) of TCR into the immune synapse may balance with TCR internalization (46) to maintain the relatively constant TCR concentration at the immune synapse assumed by the KPL-IFF model, which is consistent with previous calculations (50). A recent study has shown that changing the pMHC affinity can induce a program that over a timescale of several days changes TCR levels (51). The KPL-IFF model can explain their observation that the higher-affinity ligand induced greater TCR down-regulation if TCR levels are determined by the output of the KPL-IFF model.

The systematic analyses revealed that a large number of more complex models can explain the phenotypic features (Fig. 4*E*). This illustrates the broad challenge of (*i*) formulating unique models based on the known biochemistry and (*ii*) relating the unique model we have formulated to the known biochemistry. Limited signaling may result from modification of the TCR signalosome, such as ubiquitination (52) and/or its movement into membrane environments incompatible with signaling [e.g., endosomes (46) or microvesicles (53)] (*SI Appendix*, Fig. S7*B*). Kinetic proofreading can be realized by a number of different molecular mechanisms, such as sequential or random phosphorylation of the TCR (54, 55) and/or the recruitment of Lck-associated coreceptors (56) (*SI Appendix*, Fig. S7*A*). The incoherent feed-forward loop may result from the fact that LAT can both activate (via Grb2 and SOS) and inhibit (via Dok1/Dok2 and RasGAP) Ras (7) (*SI Appendix*, Fig. S7*C*) or from the observation that the TCR signalosome, by virtue of being able to associate with both a tyrosine kinase (ZAP-70) and a tyrosine phosphatase (SHP-1), can produce incoherent signals (2). Additionally, the positive and negative arms of the incoherent feed-forward may represent two pathways that converge to regulate cytokine production. Future work is required to map the known biochemistry onto the KPL-IFF architecture.

The systematic search for parsimonious models that can reproduce phenotypic features of cellular activation, without prior biochemical assumptions, produces signaling pathways with tractable architectures. Just as subatomic details (e.g., nuclear structure) are not necessary for atomic molecular dynamics simulations, we argue that the correct description of signaling pathways may not require detailed biochemical knowledge of individual proteins. These predictive pathway models provide a mechanistic understanding of the modular network components required to integrate input signals from the cell surface into cellular activation outputs. Although they do not include full molecular detail, they offer an intuitive framework upon which biochemical information can be mapped, which has so far been elusive with reductionist approaches.

Materials and Methods

Protein Production and Surface Plasmon Resonance. HLA-A*02:01 heavy chain (residues 1–278) with C-terminal BirA tag and β_2 -microglobulin were expressed as inclusion bodies in *Escherichia coli*, refolded in vitro in the presence of the relevant NY-ESO-$1_{156-165}$ peptide variants (*SI Appendix*, Table S1), and purified using size-exclusion chromatography. All peptides were purchased at >95% purity (GenScript). Purified pMHC was biotinylated in vitro by BirA enzyme (Avidity). The α and β subunits of the c58c61 (Clone 113) high-affinity 1G4 T-cell receptor (27) were expressed in *E. coli* as inclusion bodies, refolded in vitro, and purified using size-exclusion chromatography as described previously (17).

TCR–pMHC binding affinity and kinetics were measured by surface plasmon resonance using a Biacore 3000 (GE Healthcare) as previously described (17). Briefly, biotinylated pMHCs were coupled to the CM5 surface by covalently coupled streptavidin with a target immobilization level of 250 response units (RU) to minimize mass transport effects. The TCR analyte was diluted in HBS-EP running buffer and injected over the surface at 37 °C using a flow rate of 30 μL/min. Running buffer was injected for 4 h before the TCR injection when measuring interaction that relies on a long dissociation phase (i.e., high-affinity interactions) to ensure that baseline drifts were minimal.

The off-rate (k_{off}) was determined by fitting a one-phase exponential decay to the dissociation trace,

$$Y = (Y_0 - Y_\infty)e^{-k_{off}t} + Y_\infty,$$

where Y_0 and Y_∞ are the initial and long-time asymptotic RU, respectively. The mean k_{off} across concentrations was used to determine k_{on}. When the kinetics were such that the association phase could be resolved in time (i.e., sufficiently slow k_{off}) we fit the following one-phase exponential association to the association trace:

$$Y = \frac{[\mathrm{TCR}]B_{max}}{[\mathrm{TCR}] + K_d}\left(1 - e^{-k_{ob}t}\right),$$

where $k_{ob} = k_{on}[\mathrm{TCR}] + k_{off}$. We note that for high-affinity interactions where the dissociation trace lifetime was >15 min only a single concentration of TCR was used. Injection of multiple TCR concentrations is possible using the single-cycle kinetic mode but we found that these produced several incomplete association traces resulting in larger variability in k_{on} between experiments. We note that multiple analyte concentrations are particularly critical to determine the stoichiometry of the interaction. When the kinetics were such that the association phase could not be resolved in time (i.e., fast k_{off}) we fit the following Langmuir binding equation to the steady-state response units to obtain an estimate for K_d:

$$Y_{ss} = \frac{[\mathrm{TCR}] \times B_{max}}{K_d + [\mathrm{TCR}]},$$

where Y_{ss} is the steady-state RU. The on-rate is determined using $k_{on} = k_{off}/K_d$. All data fitting was performed in Prism (GraphPad).

Production of Lentivirus for Transduction. HEK 293T cells were seeded into 175-cm^2 flasks 24 h before transfection to achieve 50–80% confluency on the day of transfection. Cells were cotransfected with the respective third-generation lentiviral transfer vectors and packaging plasmids using a standard PEI (polyethylenimine) transfection protocol as follows. The medium was replaced with serum-free DMEM. Transfer vector and the packaging plasmid mix (17.5 μg of pRSV-rev and pMDLg/pRRE as well as 6.8 μg of pVSV-G) were diluted in 400 μL of serum-free DMEM and a dilution of 112 μg PEI in serum-free DMEM was prepared in another tube. Both were mixed vigorously and incubated at room temperature for 20 min. The mixture was added dropwise to the cells, which were then incubated at 37 °C in 10% CO_2 for 4–5 h. Afterward, the medium was replaced with complete medium. The supernatant was harvested and filtered through a 0.45-μm cellulose acetate filter 24 h later. Lentiviral particles were concentrated using Lentipac Lentivirus concentrator (GeneCopoeia) according to the manufacturer's protocol.

Transduction of Jurkat T Cells. The Jurkat E6.1 T-cell line expressing the NFAT/AP-1 luciferase reporter and CD8α (57) were transduced with the c58c61 TCR. To do this, 3 million cells were resuspended in 2 mL of concentrated virus followed by centrifugation at 2,095 × *g* for 1–2 h. The cells were incubated at 32 °C for 3.5–6 h and then cultured at 37 °C in 10% CO_2 in DMEM supplemented with 10% (vol/vol) FBS, 100 U/mL penicillin, and 100 μg/mL streptomycin.

Isolation and Transduction of Primary T Cells. Peripheral blood mononuclear cells (PBMCs) were isolated from healthy donor blood by density gradient centrifugation: Blood collected in heparinized tubes was diluted 1:2 with PBS, carefully layered onto Ficoll-Paque in 50-mL tubes and spun without brake at 400 × *g* at room temperature for 30 min. The PBMCs were collected from the interphase, spun at 520 × *g* for 5 min, and washed once with PBS.

$CD8^+$ T cells were isolated from PBMCs using the Dynabeads Untouched Human CD8 T Cells kit (Life Technologies) following the manufacturer's instructions. Briefly, PBMCs were resuspended in isolation buffer (0.1% BSA and 2 mM EDTA in PBS), blocked with FBS, and unwanted cells were labeled with an antibody mix (containing biotinylated antibodies for human CD4, CD14, CD16, CD19, CD36, CD56, CDw123, and CD235a). Subsequently, the PBMCs were washed and incubated with streptavidin-coated Dynabeads. The suspension was resuspended thoroughly with isolation buffer before the tube was placed into a magnet. The supernatant containing "untouched" $CD8^+$ T cells was collected. This process was repeated twice and the supernatants were combined.

The isolated $CD8^+$ T cells were spun at 520 × *g* for 5 min and resuspended at a concentration of 10^6 cells per mL in completely reconstituted DMEM, supplemented with 50 units/mL IL-2 and 10^6 CD3/CD28-coated Human T-Activator Dynabeads (Life Technologies) per mL. Cells were cultured at 37 °C in 10% CO_2 overnight.

The next day, 10^6 purified primary human $CD8^+$ T cells in 1 mL of medium were transduced with 1 mL of concentrated virus supplemented with 50 units of IL-2. The cells were cultured at 37 °C in 10% CO_2 and the medium was replaced with fresh medium containing 50 units/mL IL-2 every 2–3 d. CD3/CD28-coated Dynabeads were removed on day 5 after lentiviral transduction and the cells were characterized and used for experiments once the populations expanded to adequate sizes.

T-Cell Stimulation. Streptavidin-coated 96-well plates (Sigma-Aldrich) were washed two times with PBS 0.05% Tween followed by one time with PBS. Plates were incubated at 37 °C with PBS and 1% BSA for 1 h. Serially diluted pMHCs (in PBS) were transferred to the plates and incubated at 4 °C for 90 min (volume of 100 μL per well). Plates were washed three times with PBS following incubation. Plates were always prepared in pairs so that one plate could be used for the stimulation assay and the other to determine the levels of correctly folded plate-immobilized pMHC.

T-cell stimulation assays were performed by first washing and resuspending the cells in culture media without IL-2. T cells were then added at 50,000 cells per well in a volume of 100 μL. Plates were spun at 9 × *g* (4 min) and then incubated at 37 °C in 10% CO_2 for the required stimulation time.

Concentrations of supernatant cytokines were determined using commercially available ELISA kits following manufacturers' protocols: OptEIA IFN-γ (555142; BD Biosciences) and second Generation Ready-Set Go! Kits (Ebioscience) for MIP-1β (88-7034-88) and IL-8 (88-8086-88). Measurement of AP1/NFAT activity in Jurkats was performed by lysing cells using ONE-Glo Luciferase substrate (E6110; Promega) for 5 min before luminescence was read using a PherastarPlus plate reader (BMG Lab Tec). Data were corrected for background luminescence using unstimulated cells.

Levels of active plate-immobilized pMHCs were measured on the second plate using mouse anti-human HLA class I antibody (Clone W6/32, 14-9983; Ebioscience) in combination with fluorescent secondary goat anti-mouse IgG IRDye 800CW antibody (926-32210; LI-COR). Fluorescence measurements were performed with the Odyssey Imaging system (LI-COR). A Hill function was fit to the fluorescence over the initial pMHC concentration (in micrograms per milliliter) to determine the EC_{50} for each pMHC using Prism. The pMHC concentrations in the functional assays were modified to reflect differences in the immobilization EC_{50} as follows: $\log[\mathrm{pMHC}]^{corrected} = \log[\mathrm{pMHC}] + (\log(EC_{50}^{index}) - \log(EC_{50}))$ where the 9V pMHC ligand served as the index.

Flow Cytometry Assays.

Intracellular cytokine staining. T-cell stimulation was performed as described above except that 50 μL of medium supplemented with Brefeldin A (2.5 μg/mL final concentration) was added to the respective samples followed by spinning at 520 × *g* for 5 min before returning the cells to the incubator for another 2 h (primary T cells, 4-h total stimulation) or for another 3 h (Jurkat T cells, 8-h total stimulation).

After stimulation, cells were spun at 520 × *g* for 5 min and resuspended with 2 mM EDTA in PBS. After an additional spin, the cell pellets were fixed by resuspension in 50 μL per well 4% (vol/vol) formaldehyde in cold PBS at 4 °C (10 min). Fixed cells were washed with PBS, spun down at 520 × *g* for 10 min, and resuspended in 100 μL per well permeabilization buffer [PBS with 2% (wt/vol) BSA and 0.1% Triton X-100]. After 10 min at 4 °C, cells were spun at 520 × *g* for 10 min and resuspended in permeabilization buffer containing the respective antibody (E8N1 APC-conjugated IL-8 antibody or 4S. B3 AlexaFluro647 conjugated IFN-γ antibody; BioLegend) for 20 min at 4 °C. After washing twice with PBS (520 × *g* for 10 min), cells were resuspended in 100–150 μL PBS per sample and transferred into FACS tubes for analysis. Jurkat cells had to be spun before the transfer to mitigate cell losses.

Annexin V assay. Jurkat T cells were stimulated as described above except that 100,000 cells were used per well. After 16 h of stimulation, cells were removed first by gently pipetting them out of each well and second by washing each well with PBS. Cells were transferred to 1.5-mL tubes and washed two times with PBS. Cells were resuspended in annexin-V buffer (10 mM Hepes, pH 7.4, 140 mM NaCl, and 2.5 mM $CaCl_2$) at a concentration of 1–5 $\times 10^6$ cells per mL. Cells were stained with PE-Annexin-V (556421; BD Biosciences) at a concentration of 5 μL per 100 μL cells and incubated at room temperature in the dark for 15 min. After washing twice with PBS, samples were ready for flow cytometry.

c58c61 T-cell receptor expression. 5×10^5 T cells per sample were washed with PBS in FACS tubes (3 mL, 5 min at 520 × *g*) and stained with high-affinity 9V pMHC (7 μg/mL; 200 μL per sample) for 30 min. Subsequently, they were washed with PBS and stained with R-PE-conjugated streptavidin (STAR4A, 1:100; 200 μL per sample; AbD Serotec) for another 30 min. After washing twice with PBS, samples were ready for flow cytometry.

All flow cytometry was performed using a FACSCalibur (BD Biosciences) with at least 10,000 cells. All analysis was performed using the software FlowJo (TreeStar).

ACKNOWLEDGMENTS. We thank Gillian Griffiths, Paul Francois, Arup Chakraborty, John R. James, and Bela Novak for feedback during the development of the work; Georg Kempf, Marcus Bridge, Nathan Jenko, Ann Tivey, and Dhruv Jayanth for assistance in protein production and kinetic measurements; and Simon J. Davis for a critical reading of the manuscript. The c58c61 TCR was provided by Adaptimmune Ltd. This work was supported by a Doctoral Training Centre Systems Biology studentship from the Engineering and Physical Sciences Research Council (to M.L. and N.T.), Wellcome Trust Senior Investigator Award Grant 101799 (to P.A.v.d.M.), and a Sir Henry Dale Fellowship jointly funded by the Wellcome Trust and Royal Society Grant 098363 (to O.D.).

1. Smith-Garvin JE, Koretzky GA, Jordan MS (2009) T cell activation. *Annu Rev Immunol* 27:591–619.
2. Altan-Bonnet G, Germain RN (2005) Modeling T cell antigen discrimination based on feedback control of digital ERK responses. *PLoS Biol* 3(11):e356.
3. Dushek O, van der Merwe PA (2014) An induced rebinding model of antigen discrimination. *Trends Immunol* 35(4):153–158.
4. Turner MS, Kane LP, Morel PA (2009) Dominant role of antigen dose in CD4+Foxp3+ regulatory T cell induction and expansion. *J Immunol* 183(8):4895–4903.
5. Gottschalk RA, Corse E, Allison JP (2010) TCR ligand density and affinity determine peripheral induction of Foxp3 in vivo. *J Exp Med* 207(8):1701–1711.
6. Acuto O, Di Bartolo V, Michel F (2008) Tailoring T-cell receptor signals by proximal negative feedback mechanisms. *Nat Rev Immunol* 8(9):699–712.
7. Brownlie RJ, Zamoyska R (2013) T cell receptor signalling networks: branched, diversified and bounded. *Nat Rev Immunol* 13(4):257–269.
8. Corse E, Gottschalk RA, Allison JP (2011) Strength of TCR-peptide/MHC interactions and in vivo T cell responses. *J Immunol* 186(9):5039–5045.
9. Lever M, Maini PK, van der Merwe PA, Dushek O (2014) Phenotypic models of T cell activation. *Nat Rev Immunol* 14(9):619–629.
10. Kalergis AM, et al. (2001) Efficient T cell activation requires an optimal dwell-time of interaction between the TCR and the pMHC complex. *Nat Immunol* 2:229–34.
11. Coombs D, Kalergis AM, Nathenson SG, Wofsy C, Goldstein B (2002) Activated TCRs remain marked for internalization after dissociation from pMHC. *Nat Immunol* 3(10):926–931.
12. Holler PD, Kranz DM (2003) Quantitative analysis of the contribution of TCR/pepMHC affinity and CD8 to T cell activation. *Immunity* 18(2):255–264.
13. González PA, et al. (2005) T cell receptor binding kinetics required for T cell activation depend on the density of cognate ligand on the antigen-presenting cell. *Proc Natl Acad Sci USA* 102(13):4824–4829.
14. McMahan RH, et al. (2006) Relating TCR-peptide-MHC affinity to immunogenicity for the design of tumor vaccines. *J Clin Invest* 116(9):2543–2551.
15. Chervin AS, et al. (2009) The impact of TCR-binding properties and antigen presentation format on T cell responsiveness. *J Immunol* 183(2):1166–1178.
16. Schmid Da, et al. (2010) Evidence for a TCR affinity threshold delimiting maximal CD8 T cell function. *J Immunol* 184:4936–4946.
17. Aleksic M, et al. (2010) Dependence of T cell antigen recognition on T cell receptor-peptide MHC confinement time. *Immunity* 32(2):163–174.
18. Govern CC, Paczosa MK, Chakraborty AK, Huseby ES (2010) Fast on-rates allow short dwell time ligands to activate T cells. *Proc Natl Acad Sci USA* 107(19):8724–8729.
19. Corse E, Gottschalk RA, Krogsgaard M, Allison JP (2010) Attenuated T cell responses to a high-potency ligand in vivo. *PLoS Biol* 8(9):1–12.
20. Thomas S, et al. (2011) Human T cells expressing affinity-matured TCR display accelerated responses but fail to recognize low density of MHC-peptide antigen. *Blood* 118(2):319–329.
21. Dushek O, et al. (2011) Antigen potency and maximal efficacy reveal a mechanism of efficient T cell activation. *Sci Signal* 4(176):ra39.
22. Irving M, et al. (2012) Interplay between T cell receptor binding kinetics and the level of cognate peptide presented by major histocompatibility complexes governs CD8+ T cell responsiveness. *J Biol Chem* 287(27):23068–23078.
23. Lee HM, Bautista JL, Scott-Browne J, Mohan JF, Hsieh CS (2012) A broad range of self-reactivity drives thymic regulatory T cell selection to limit responses to self. *Immunity* 37(3):475–486.
24. Tan MP, et al. (2015) T cell receptor binding affinity governs the functional profile of cancer-specific CD8+ T cells. *Clin Exp Immunol* 180(2):255–270.
25. Restifo NP, Dudley ME, Rosenberg SA (2012) Adoptive immunotherapy for cancer: Harnessing the T cell response. *Nat Rev Immunol* 12(4):269–281.
26. Jakka G, et al. (2013) Antigen-specific in vitro expansion of functional redirected NY-ESO-1-specific human CD8+ T-cells in a cell-free system. *Anticancer Res* 33(10):4189–4201.
27. Li Y, et al. (2005) Directed evolution of human T-cell receptors with picomolar affinities by phage display. *Nat Biotechnol* 23(3):349–354.
28. Chmielewski M, Hombach A, Heuser C, Adams GP, Abken H (2004) T cell activation by antibody-like immunoreceptors: Increase in affinity of the single-chain fragment domain above threshold does not increase T cell activation against antigen-positive target cells but decreases selectivity. *J Immunol* 173(12):7647–7653.
29. Haso W, et al. (2013) Anti-CD22-chimeric antigen receptors targeting B-cell precursor acute lymphoblastic leukemia. *Blood* 121(7):1165–1174.
30. Caruso HG, et al. (2015) Tuning sensitivity of CAR to EGFR density limits recognition of normal tissue while maintaining potent antitumor activity. *Cancer Res* 75(17):3505–3518.
31. Sadelain M, Brentjens R, Rivière I (2009) The promise and potential pitfalls of chimeric antigen receptors. *Curr Opin Immunol* 21(2):215–223.
32. Aldridge BB, Burke JM, Lauffenburger DA, Sorger PK (2006) Physicochemical modelling of cell signalling pathways. *Nat Cell Biol* 8(11):1195–1203.
33. Gunawardena J (2014) Models in biology: 'Accurate descriptions of our pathetic thinking'. *BMC Biol* 12:29.
34. Schmidt M, Lipson H (2009) Distilling free-form natural laws from experimental data. *Science* 324(5923):81–85.
35. Ma W, Trusina A, El-Samad H, Lim WA, Tang C (2009) Defining network topologies that can achieve biochemical adaptation. *Cell* 138(4):760–773.
36. Shah NA, Sarkar CA (2011) Robust network topologies for generating switch-like cellular responses. *PLOS Comput Biol* 7(6):e1002085.
37. François P (2014) Evolving phenotypic networks in silico. *Semin Cell Dev Biol* 35:90–97.
38. Villaverde AF, Banga JR (2013) Reverse engineering and identification in systems biology: Strategies, perspectives and challenges. *J R Soc Interface* 11(91):20130505.
39. Daniels BC, Nemenman I (2014) Automated adaptive inference of coarse-grained dynamical models in systems biology. *Nat Commun* 6:38.
40. Sami M, et al. (2007) Crystal structures of high affinity human T-cell receptors bound to peptide major histocompatibility complex reveal native diagonal binding geometry. *Protein Eng Des Sel* 20(8):397–403.
41. Adams JJ, et al. (2016) Structural interplay between germline interactions and adaptive recognition determines the bandwidth of TCR-peptide-MHC cross-reactivity. *Nat Immunol* 17(1):87–94.
42. Green DR, Droin N, Pinkoski M (2003) Activation-induced cell death in T cells. *Immunol Rev* 193:70–81.
43. Alon U (2007) Network motifs: Theory and experimental approaches. *Nat Rev Genet* 8(6):450–461.
44. Toni T, Welch D, Strelkowa N, Ipsen A, Stumpf MP (2009) Approximate Bayesian computation scheme for parameter inference and model selection in dynamical systems. *J R Soc Interface* 6(31):187–202.
45. Krogsgaard M, Juang J, Davis MM (2007) A role for "self" in T-cell activation. *Semin Immunol* 19(4):236–244.
46. Valitutti S, Müller S, Cella M, Padovan E, Lanzavecchia A (1995) Serial triggering of many T-cell receptors by a few peptide-MHC complexes. *Nature* 375(6527):148–151.
47. Moss WC, Irvine DJ, Davis MM, Krummel MF (2002) Quantifying signaling-induced reorientation of T cell receptors during immunological synapse formation. *Proc Natl Acad Sci USA* 99(23):15024–15029.
48. Das V, et al. (2004) Activation-induced polarized recycling targets T cell antigen receptors to the immunological synapse; involvement of SNARE complexes. *Immunity* 20(5):577–588.
49. Finetti F, et al. (2014) Specific recycling receptors are targeted to the immune synapse by the intraflagellar transport system. *J Cell Sci* 127(Pt 9):1924–1937.

50. Arkhipov SN, Maly IV (2006) Quantitative analysis of the role of receptor recycling in T cell polarization. *Biophys J* 91(11):4306–4316.
51. Gallegos AM, et al. (2016) Control of T cell antigen reactivity via programmed TCR downregulation. *Nat Immunol* 17(4):379–386.
52. Yang M, et al. (2015) K33-linked polyubiquitination of Zap70 by Nrdp1 controls CD8 (+) T cell activation. *Nat Immunol* 16(12):1253–1262.
53. Choudhuri K, et al. (2014) Polarized release of T-cell-receptor-enriched microvesicles at the immunological synapse. *Nature* 507(7490):118–123.
54. McKeithan TW (1995) Kinetic proofreading in T-cell receptor signal transduction. *Proc Natl Acad Sci USA* 92(11):5042–5046.
55. Mukhopadhyay H, et al. (2016) Multisite phosphorylation modulates the T cell receptor ζ-chain potency but not the switchlike response. *Biophys J* 110(8):1896–1906.
56. Stepanek O, et al. (2014) Coreceptor scanning by the T cell receptor provides a mechanism for T cell tolerance. *Cell* 159(2):333–345.
57. Paster W, et al. (2015) A THEMIS:SHP1 complex promotes T-cell survival. *EMBO J* 34(3): 393–409.

Supporting Information

Lever et al. 10.1073/pnas.1608820113

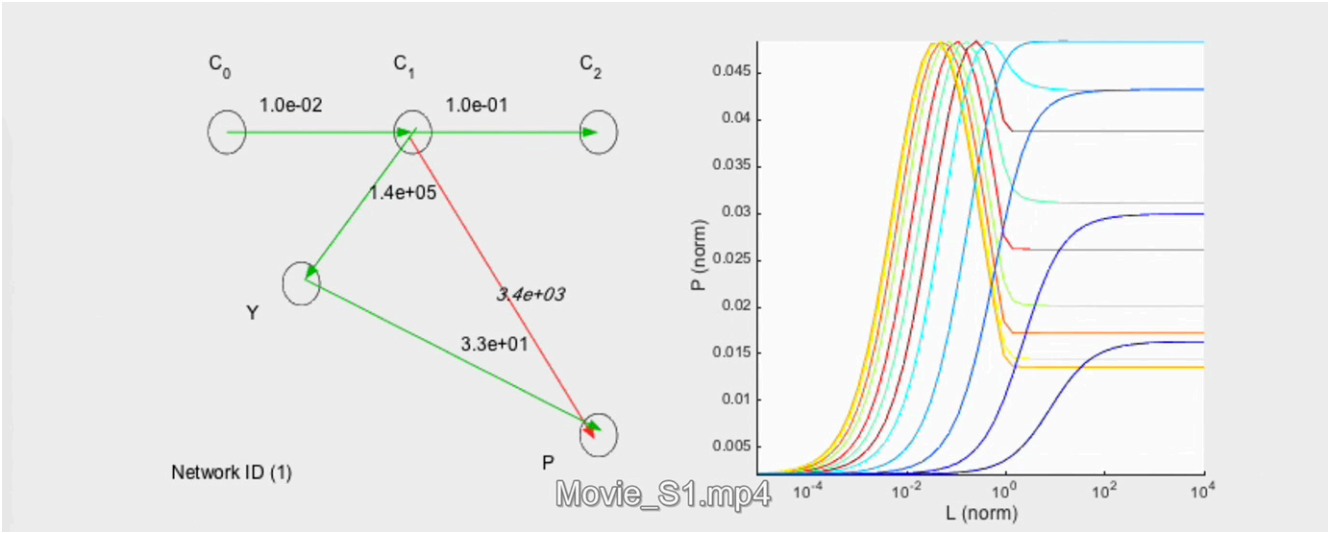

Movie S1. Systematic analysis of 304 network architectures (Fig. 4*A*). Each 1-s frame shows the network architecture (*Left*) and the network output (*Right*). The network architecture displays the three receptor states (C_0, C_1, and C_2) together with *Y* and *P*, where green arrows indicate activation and red arrows indicate inhibition (magnitudes of inhibition arrows are in italics). The network output displays *P* (*y* axis) over the ligand concentration (*x* axis) for ligands with decreasing k_{off} (blue to red). Networks appear in ascending order of the sum of squared residuals (SSR) so that networks that are better able to produce the phenotypic features appear first. See *SI Appendix* for computational details.

Movie S1

Other Supporting Information Files

SI Appendix (PDF)

Supplementary Information Appendix: Architecture of a minimal signalling pathway explains the T cell response to a 1,000,000-fold variation in antigen affinity and dose

Melissa Lever[†*], Hong-Sheng Lim[†*], Philipp Kruger[†*], John Nguyen[†], Nicola Trendel[†], Enas Abu-Shah[†], Philip Kumar Maini[‡], Philip Anton van der Merwe[†], Omer Dushek[†,‡,¶]

[†]Sir William Dunn School of Pathology, University of Oxford, Oxford, United Kingdom
[‡]Wolfson Centre for Mathematical Biology, Mathematical Institute, University of Oxford, Oxford, United Kingdom
[*]These authors contributed equally
[¶]Corresponding author

Supplementary Text

Phenotypic model equations (KPL-IFF)

The ordinary-differential-equations (ODEs) corresponding to kinetic proofreading with limited signalling coupled to incoherent feedforward (KPL-IFF, Figure 3d) are,

$$\begin{aligned}
\mathrm{d}L/\mathrm{d}t &= -k_{\text{on}}LR + k_{\text{off}}(C_0 + C_1 + C_2) \\
\mathrm{d}R/\mathrm{d}t &= -k_{\text{on}}LR + k_{\text{off}}(C_0 + C_1 + C_2) \\
\mathrm{d}C_0/\mathrm{d}t &= k_{\text{on}}LR - (k_{\text{off}} + k_{\text{p}})C_0 \\
\mathrm{d}C_1/\mathrm{d}t &= k_{\text{p}}C_0 - (k_{\text{off}} + \phi k_{\text{p}})C_1 \\
\mathrm{d}C_2/\mathrm{d}t &= \phi k_{\text{p}}C_1 - k_{\text{off}}C_2 \\
\mathrm{d}Y/\mathrm{d}t &= \gamma_+^y(Y_T - Y) - \gamma_-^y Y + \lambda C_1(Y_T - Y) \\
\mathrm{d}P/\mathrm{d}t &= \gamma_+^p(P_T - P) - \gamma_-^p P + \delta Y(P_T - P) - \mu C_1 P
\end{aligned}$$

where k_{on} and k_{off} are the TCR-pMHC kinetic rate constants, k_{p} is the kinetic proofreading rate, ϕ is the limited signalling parameter, λ is the amplification parameter, μ is the inhibition parameter, and δ is the activation

parameter. We solve the system in the steady-state to obtain the following,

$$\begin{aligned}
\hat{C}_0 &= \left(\frac{k_{\text{off}}}{k_{\text{off}}+k_{\text{p}}}\right)\hat{C}_T \\
\hat{C}_1 &= \left(\frac{k_{\text{off}}}{k_{\text{off}}+k_{\text{p}}}\right)\left(\frac{k_{\text{p}}}{k_{\text{off}}+\phi k_{\text{p}}}\right)\hat{C}_T \\
\hat{C}_2 &= \left(\frac{\phi k_{\text{p}}}{k_{\text{off}}+k_{\text{p}}}\right)\left(\frac{k_{\text{p}}}{k_{\text{off}}+\phi k_{\text{p}}}\right)\hat{C}_T \\
\hat{Y} &= \frac{1+\hat{\lambda}\hat{C}_1}{1+\hat{\lambda}\hat{C}_1+\hat{\gamma}^y} \\
\hat{P} &= \frac{1+\hat{\delta}\hat{Y}}{1+\hat{\delta}\hat{Y}+\hat{\gamma}^p+\hat{\mu}\hat{C}_1}
\end{aligned}$$

with

$$\hat{C}_T = \left((L_T/R_T+1+k_{\text{off}}/k_{\text{on}}R_T)-\sqrt{(L_T/R_T+1+k_{\text{off}}/k_{\text{on}}R_T)^2-4L_T/R_T}\right)/2$$

where we have used 'hat' quantities to represent nondimensionalized concentrations and parameters: $\hat{C}_T = C_T/R_T$, $\hat{C}_0 = C_0/R_T$, $\hat{C}_1 = C_1/R_T$, $\hat{C}_2 = C_2/R_T$, $\hat{Y} = Y/Y_T$, $\hat{P} = P/P_T$, $\hat{\lambda} = \lambda R_T/\gamma_+^y$, $\hat{\gamma}^y = \gamma_-^y/\gamma_+^y$, $\hat{\delta} = \delta Y_T/\gamma_+^p$, $\hat{\gamma}^p = \gamma_-^p/\gamma_+^p$ and $\hat{\mu} = \mu R_T/\gamma_+^p$.

The model calculations in Figure 3d were generated using $k_{\text{p}} = 0.01$ s^{-1}, $\phi = 0.1$, $\hat{\gamma^p} = \hat{\gamma^y} = 500$, $k_{\text{on}}R_T = 1$, $\hat{\lambda} = 10000$, $\hat{\delta} = 5000$, and $\hat{\mu} = 50000$ with the indicated variation of L_T/R_T (x-axis) and a variation of k_{off} from 10^{-4} to 10^2 s^{-1} (coloured lines). We provide a web applet that can be used to examine the predicted dose-response from this phenotypic model for any parameter values (Applet S1).

Systematic analysis of phenotypic model network architectures

The key objective of the systematic analysis is to determine whether other models can also produce the key features that the kinetic proofreading with limited signalling coupled to incoherent feedforward (KPL-IFF) model is able to produce (Figure 3d, Table 1).

We performed two systematic analyses of phenotypic models: a simpler systematic analysis looking at 304 networks (Figure 4a) and a more complex analysis looking at 26,069 networks (Figure 4e). Given that the methodology is identical for both analyses and that the simpler analysis is nested within the more complex analysis, this section will focus on describing the more complex analysis. The methodology extends previous efforts to systematically study pre-defined network architectures that can produce specific phenotypes (1, 2).

Defining the set of network architectures. The set network architectures that we examine are defined based on the possible reactions that we consider. Each network has a receptor that can undergo kinetic proofreading with 4 steps (C_0, C_1, C_2, and C_3) and 3 additional nodes (X, Y, and P). We consider all possible networks that have 4 reaction arrows (either activating or inhibiting) between the receptor, X, Y, and P (Figure 4d). Note that every network contains the 4 kinetic proofreading states. The total number of reaction arrows is 36 and therefore the total number of networks is 58,905 (36 choose 4). Without loss of generality we identify P as the output and remove all networks where there is no connection between any of the kinetic proofreading states and P (either directly or indirectly), which reduces the number of networks to 26,069. We omit networks where X, Y, or P modulate kinetic proofreading to maintain computational feasibility. Each network contains a total of 6 free parameters; 2 kinetic proofreading parameters (k_{p} and ϕ) and 1 parameter for each of the 4 reaction arrows.

A scale-free comparison measure. The large number of networks that are to be systematically examined means that it is not feasible to manually identify (i.e. by eye) whether a specific proposed network can also produce the output of the KPL-IFF network (Figure 3d). To automate identification we constructed a quantitative measure that can compare the output of the KPL-IFF network to a specific proposed network.

First, we define four elementary numbers for any dose-response curve (Figure S4a): the value of P at the lowest concentration (W_1), the maximum value of P (W_2), the value of P at the largest concentration (W_3), and the concentration of ligand producing half-maximal response (EC_{50}). In cases where two values of EC_{50} are possible the lower value is used (i.e. to the left of the peak in a bell-shaped dose-response).

Second, we define four metrics that capture the key qualitative features of the KPL-IFF output,

$$\begin{aligned} F_1 &= W_1/W_2 \\ F_2 &= (W_3/W_2)/(W_3^*/W_2^*) \\ F_3 &= W_2/W_2^* \\ F_4 &= EC_{50}/EC_{50}^* \end{aligned}$$

where the superscript $*$ refers to the values for an index ligand, which we take to be the highest affinity ligand. These four metrics can be calculated for each ligand and plotted as a function of the ligand k_{off} value for the KPL-IFF network (Figure S4b-g). The first measure (F_1) ensures that the dose-response curve exhibits an increase. The second measure (F_2) ensures that a bell-shaped dose-response is observed. The third measure (F_3) ensures that the peak height is similar for high affinity ligands but decreases for low affinity ligands. The fourth measure (F_4) ensures that ligands of intermediate affinity are first to increase as a function of dose. The normalisation to an index ligand means that these measures are largely independent of the absolute values of L (dose) and P (response). Note that these measures rely on fold-changes and therefore are independent of the absolute scale of the response (value of P).

Lastly, we define a single measure that can compare the similarity between F_1, F_2, F_3, and F_4 (across a wide range of k_{off} values) for any specific network and the KPL-IFF network,

$$\text{SSR} = \sum_{i=1}^{N} (F_1^i - \widehat{F}_1^i)^2 + (F_2^i - \widehat{F}_2^i)^2 + (F_3^i - \widehat{F}_3^i)^2 + (F_4^i - \widehat{F}_4^i)^2 \tag{1}$$

where the index i represents each ligand ($i = 1$ to $i = N$ ligands with $N = 12$ in our example). The values of F with a hat represent those for the KPL-IFF network whereas the non-hat values are for the specific network being tested.

In summary, the output of any proposed network are the values of P as a function of ligand concentrations for 12 ligands with different values of k_{off}. This output is used to calculate F_1, F_2, F_3, and F_4 for each ligand which can then be used to compute SSR. Proposed networks with small SSR values are more likely to be compatible with the output of the KPL-IFF network and therefore the key features.

Workflow. The workflow for the systematic analysis is shown in Figure S4h. The first step is to select one of the 26,069 networks to analyse. The next two steps aim to determine the values of the 6 model parameters that produce the smallest value of the SSR for the selected network. First, the method performs 1 million evaluations of the network where the 6 model parameters for each evaluation are randomly sampled (uniform distribution in log-space) and the SSR for each evaluation is determined. Second, the values of the 6 parameters for the 15 network evaluations that produced the smallest values of SSR (from the 1 million that were sampled) are then used as initial conditions for a non-linear optimisation algorithm (*fminsearch* in Matlab) that uses a modified simplex method to further minimize the SSR. Finally, the 6 parameter values that produced the smallest SSR (among the 15 optimised parameter values) are recorded along with the associated SSR for the network. The procedure is repeated for all 26,069 networks.

Given that the analysis relies on two steps that have a stochastic element (random parameter sampling and further optimisation) we repeated the analysis 3 times for both the simpler and complex analysis but found no difference to the results (see below) suggesting that the search algorithm had sufficient coverage of parameter space.

Results. The output of the analysis is a list of the 26,069 networks (or the 304 networks for the simpler analysis) ordered from the smallest to the largest SSR. We summarise this output in Movie S2 (or Movie S1 for the simpler analysis) where each 1 second frame corresponds to a network architecture evaluated with the 6 optimised parameter values. By examining the movies we find that 274 of the 26,069 networks in the complex analysis (or 1 of the 304 networks in the simpler analysis) are compatible with the key features as they are able to reproduce the output of the KPL-IFF network. Importantly, all 274 compatible networks contained the same underlying KPL-IFF mechanism. In many cases these more complex networks were reduced to the same KPL-IFF model shown in Figure 3d (e.g. networks 2, 4, 7 to 21, etc) whilst in other cases the incoherent feedforward exhibited indirect inhibition (e.g. networks 1, 3, 5, 6, etc) but operated in a parameter regime where inhibition saturated after activation.

Mathematical model. The systematic analysis relies on evaluating many network architectures. To do this, we have implemented a single general mathematical model that can be reduced to all 26,069 networks by setting appropriate reactions to zero.

The ordinary-differential-equations (ODEs) corresponding to the most general mathematical model are,

$$
\begin{aligned}
\mathrm{d}L/\mathrm{d}t &= -k_{\text{on}}LR + k_{\text{off}}C_T \\
\mathrm{d}R/\mathrm{d}t &= -k_{\text{on}}LR + k_{\text{off}}C_T \\
\mathrm{d}C_0/\mathrm{d}t &= k_{\text{on}}LR - (k_{\text{off}} + k_{\text{p}})C_0 \\
\mathrm{d}C_i/\mathrm{d}t &= k_{\text{p}}C_{i-1} - (k_{\text{p}} + k_{\text{off}})C_i \quad 1 \leq i < N-1 \\
\mathrm{d}C_N/\mathrm{d}t &= k_{\text{p}}C_{N-1} - (k_{\text{off}} + \phi k_{\text{p}})C_N \\
\mathrm{d}C_{N+1}/\mathrm{d}t &= \phi k_{\text{p}}C_N - k_{\text{off}}C_{N+1} \\
\mathrm{d}X/\mathrm{d}t &= \gamma_+^x(X_T - X) - \gamma_-^x X \\
&\quad +(\vec{\lambda}^x \cdot \vec{C})(X_T - X) - (\vec{\mu}^x \cdot \vec{C})X \\
&\quad +(\eta_+^y Y + \eta_+^p P)(X_T - X) - (\eta_-^y Y + \eta_-^p P)X \\
\mathrm{d}Y/\mathrm{d}t &= \gamma_+^y(Y_T - Y) - \gamma_-^y Y \\
&\quad +(\vec{\lambda}^y \cdot \vec{C})(Y_T - Y) - (\vec{\mu}^y \cdot \vec{C})Y \\
&\quad +(\beta_+^x X + \beta_+^p P)(Y_T - Y) - (\beta_-^x X + \beta_-^p P)Y \\
\mathrm{d}P/\mathrm{d}t &= \gamma_+^p(P_T - P) - \gamma_-^p P \\
&\quad +(\vec{\lambda}^p \cdot \vec{C})(P_T - P) - (\vec{\mu}^p \cdot \vec{C})P \\
&\quad +(\delta_+^x X + \delta_+^y Y)(P_T - P) - (\delta_-^x X + \delta_-^y Y)P
\end{aligned}
$$

where $C_T = \sum_{i=0}^{N+1} C_i$ and $\vec{\lambda}^x \cdot \vec{C}$ is the vector dot product between the parameter vector ($\vec{\lambda}^x = [\lambda_0^x, \lambda_1^x, ...\lambda_{N+1}^x]$) and the vector of complexes ($\vec{C} = [C_0, C_1, ..., C_{N-1}, C_N, C_{N+1}]$). We solve the ODE system in the steady-state

to obtain,

$$\begin{aligned} C_0 &= \alpha^0(1-\alpha)C_T \\ C_1 &= \alpha^1(1-\alpha)C_T \\ &\vdots \\ C_{N-1} &= \alpha^{(N-1)}(1-\alpha)C_T \\ C_N &= \alpha^N\left(\frac{k_{\text{off}}}{k_{\text{off}}+\phi k_{\text{p}}}\right)C_T \\ C_{N+1} &= \alpha^N\left(\frac{\phi k_{\text{p}}}{k_{\text{off}}+\phi k_{\text{p}}}\right)C_T \end{aligned}$$

where

$$\begin{aligned} \frac{C_T}{R_T} &= \left(\frac{L_T}{R_T}+1+\frac{k_{\text{off}}}{k_{\text{on}}R_T}-\sqrt{\left(\frac{L_T}{R_T}+1+\frac{k_{\text{off}}}{k_{\text{on}}R_T}\right)^2-4\frac{L_T}{R_T}}\right)/2, \\ \alpha &= \frac{k_{\text{p}}}{k_{\text{off}}+k_{\text{p}}}, \end{aligned}$$

and the equations for X, Y, and P simplify to,

$$\begin{aligned} 0 &= (1-X)-\gamma_m^x X+(\vec{\lambda}_m^x\cdot\vec{C})(1-X)-(\vec{\mu}_m^x\cdot\vec{C})X+(\alpha_{+m}^y Y+\alpha_{+m}^p P)(1-X)-(\eta_{-m}^y Y+\eta_{-m}^p P)X \\ 0 &= (1-Y)-\gamma_m^y Y+(\vec{\lambda}_m^y\cdot\vec{C})(1-Y)-(\vec{\mu}_m^y\cdot\vec{C})Y+(\beta_{+m}^x X+\beta_{+m}^p P)(1-Y)-(\beta_{-m}^x X+\beta_{-m}^p P)Y \\ 0 &= (1-P)-\gamma_m^p P+(\vec{\lambda}_m^p\cdot\vec{C})(1-P)-(\vec{\mu}_m^p\cdot\vec{C})P+(\delta_{+m}^x X+\delta_{+m}^y Y)(1-P)-(\delta_{-m}^x X+\delta_{-m}^y Y)P \end{aligned}$$

where we have nondimensionalized concentrations (R by R_T, C_i by R_T, X by X_T, Y by Y_T, and P by P_T) but retained original notation for clarity. The subscript m indicates that the parameter has been modified as a result of the nondimensionalization process: $\gamma_m^x=\gamma_-^x/\gamma_+^x$, $\gamma_m^y=\gamma_-^y/\gamma_+^y$, $\gamma_m^p=\gamma_-^p/\gamma_+^p$, $\vec{\lambda}_m^x=\vec{\lambda}^x R_T/\gamma_+^x$, $\vec{\lambda}_m^y=\vec{\lambda}^y R_T/\gamma_+^y$, $\vec{\lambda}_m^p=\vec{\lambda}^p R_T/\gamma_+^p$, $\vec{\mu}_m^x=\vec{\mu}^x R_T/\gamma_+^x$, $\vec{\mu}_m^y=\vec{\mu}^y R_T/\gamma_+^y$, $\vec{\mu}_m^p=\vec{\mu}^p R_T/\gamma_+^p$, $\eta_{+m}^y=\eta_+^y Y_T/\gamma_+^x$, $\eta_{+m}^p=\eta_+^p P_T/\gamma_+^x$, $\eta_{-m}^y=\eta_-^y Y_T/\gamma_+^x$, $\eta_{-m}^p=\eta_-^p P_T/\gamma_+^x$, $\beta_{+m}^x=\beta_+^x X_T/\gamma_+^y$, $\beta_{+m}^p=\beta_+^p P_T/\gamma_+^y$, $\beta_{-m}^x=\beta_-^x X_T/\gamma_+^y$, $\beta_{-m}^p=\beta_-^p P_T/\gamma_+^y$, $\delta_{+m}^x=\delta_+^x X_T/\gamma_+^p$, $\delta_{+m}^y=\delta_+^y Y_T/\gamma_+^p$, $\delta_{-m}^x=\delta_-^x X_T/\gamma_+^p$, and $\delta_{-m}^y=\delta_-^y Y_T/\gamma_+^p$.

In the case of the more complex analysis (4 nodes, 4 reaction arrows) the number of kinetic proofreading steps was 4 ($N=3$). The ratio of background inhibition to background activation of X, Y, and P were fixed at 500 so that without any ligand the concentrations of X, Y, and P were near zero ($\gamma_m^x=\gamma_m^y=\gamma_m^p=500$). The remaining parameters were set to 0 with the exception of k_{p}, ϕ, and 4 other parameters that defined the network architecture. The same procedure was carried out for the simpler analysis (3 nodes, 3 reaction arrows) except that the number of kinetic proofreading steps was 3 ($N=2$) and all reactions to and from X were set to zero.

The mathematical model was numerically solved using *fzero* in Matlab (Mathworks, MA), which allowed the code to be translated to C++ by the Matlab Coder toolbox. We found that the solution converged rapidly when using 0 as the initial guess.

KPL-IFF model parameters compatible with phenotypic features

To determine the set of parameters in the KPL-IFF model (λ, δ, μ, k_{p}, ϕ) compatible with the key features we utilised Approximate Bayesian Computations with Sequential Monte Carlo (ABC-SMC) (3, 4). We used the SSR (described above) as the summary statistic and terminated the algorithm when $> 10,000$ particles were found with $SSR < 1$. Distributions of the 5 parameters along with their pairwise correlations are shown in Figure S6.

Negative feedback cannot produce a bell-shaped dose-response

The systematic analysis described in the previous section (see also main text and Fig. 4) has revealed that negative feedback, although well known to produce oscillations in time, cannot produce a bell-shaped dose-response in the steady-state. In this section we provide further evidence for this numerical result by providing an intuitive explanation together with an analytical proof.

First, consider a two component negative feedback (Figure S5a) whereby P activates Y and Y in turn inhibits P. As the activator of P increases (C_1 in this example), P will increase. In order to decrease P (to produce a bell-shaped dose-response) Y needs to inhibit P more strongly at larger values of P. But a larger value of active Y (needed for stronger inhibition of P) requires larger value of active P. Therefore, P and Y are subjected to two conflicting requirements which cannot be satisfied simultaneously. It follows that a bell-shaped dose-response for P cannot be achieved in the steady-state.

In what follows we provide a mathematical proof that a bell-shaped dose-response cannot be produced with negative feedback in the steady-state. To do this, we derive an implicit expression for P and show that the first derivative cannot be zero for any positive reaction rate constants. The non-linear coupled system of ODEs for the two component negative feedback can be written as follows,

$$\frac{\mathrm{d}\hat{Y}}{\mathrm{d}t} = \frac{\eta_+^P}{1+\left(\frac{\hat{\rho}}{\hat{P}}\right)^n} + \gamma_+^Y - \left[\frac{\eta_+^P}{1+\left(\frac{\hat{\rho}}{\hat{P}}\right)^n} + \gamma_+^Y + \gamma_-^Y\right]\hat{Y} \tag{2}$$

$$\frac{\mathrm{d}\hat{P}}{\mathrm{d}t} = (\lambda\hat{C}_1 + \gamma_+^P)(1-\hat{P}) - \hat{\beta_-^Y}\hat{Y}\hat{P} - \gamma_-^P\hat{P} \tag{3}$$

where $\hat{Y}$ and $\hat{P}$ are non-dimensional ($\hat{Y} = Y/Y_T$, $\hat{P} = P/P_T$) with $\hat{\rho} = \rho/P_T$, and $\hat{\beta_-^Y} = \beta_-^Y Y_T$. Note that all reactions considered in the main text are based on non-saturating mass action but in this analysis we have included a more general saturating inhibition, which can be reduced to mass action in the limit of large $\hat{\rho}$ with $n = 1$. In the steady-state we find,

$$\hat{Y} = \frac{(\lambda\hat{C}_1 + \gamma_+^P)(\frac{1}{\hat{P}} - 1) - \gamma_-^P}{\hat{\beta_-^Y}}$$

which, we substitute into the steady-state of equation (2) to obtain,

$$f = 1 - \left[1 + \frac{\gamma_-^Y}{\frac{\eta_+^P}{1+\left(\frac{\hat{\rho}}{\hat{P}}\right)^n} + \gamma_+^Y}\right]\left[\frac{\kappa(\frac{1}{\hat{P}} - 1) - \gamma_-^P}{\hat{\beta_-^Y}}\right] = 0 \tag{4}$$

where $\kappa = \lambda\hat{C}_1 + \gamma_+^P$ contains the input from $\hat{C}_1$. To determine if P can exhibit a bell-shaped dose-response as a function of $\hat{C}_1$ we determine the value of the parameters where the first derivative of P is zero. To do this, we differentiate P with respect to κ,

$$\frac{\mathrm{d}f}{\mathrm{d}\kappa} = -\left[\frac{-n\gamma_-^Y\eta_+^P\left(\frac{\hat{\rho}}{\hat{P}}\right)^n\frac{\mathrm{d}\hat{P}}{\mathrm{d}\kappa}}{\hat{P}\left(\frac{\eta_+^P}{1+\left(\frac{\hat{\rho}}{\hat{P}}\right)^n} + \gamma_+^Y\right)^2\left[1+\left(\frac{\hat{\rho}}{\hat{P}}\right)\right]^2}\right]\left[\frac{\kappa(\frac{1}{\hat{P}} - 1) - \gamma_-^P}{\hat{\beta_-^Y}}\right]$$
$$- \left[1 + \frac{\gamma_-^Y}{\frac{\eta_+^P}{1+\left(\frac{\hat{\rho}}{\hat{P}}\right)^n} + \gamma_+^Y}\right]\left[\frac{1}{\hat{\beta_-^Y}}\left(\frac{\hat{P} - \kappa\frac{\mathrm{d}\hat{P}}{\mathrm{d}\kappa}}{\hat{P}^2} - 1\right)\right] = 0 \tag{5}$$

At $\frac{\mathrm{d}\hat{P}}{\mathrm{d}\kappa} = 0$, equation (5) reduces to

$$-\left[1+\frac{\gamma_-^Y}{\frac{\eta_+^P}{1+\left(\frac{\hat{\rho}}{\hat{P}}\right)^n}+\gamma_+^Y}\right]\left[\frac{1}{\hat{\beta_-^Y}}\left(\frac{1}{\hat{P}}-1\right)\right]=0$$

which can be satisfied when

$$1+\frac{\gamma_-^Y}{\frac{\eta_+^P}{1+\left(\frac{\hat{\rho}}{\hat{P}}\right)^n}+\gamma_+^Y}=0 \tag{6}$$

and/or when

$$\frac{1}{\hat{\beta_-^Y}}\left(\frac{1}{\hat{P}}-1\right)=0 \tag{7}$$

Given that all reaction rate constants and concentrations must be positive it is clear that there are no values of $\hat{P}$ and reaction rate constants that satisfy equation (6). We do find that equation (7) can be satisfied when $\hat{P}=1$ (i.e. $\hat{P}$ is maximally active) but at this value of $\hat{P}$ we find that the equation for f,

$$f=1+\frac{\gamma_-^P}{\hat{\beta_-^Y}}\left[1+\frac{\gamma_-^Y}{\frac{\eta_+^P}{1+\hat{\rho}^n}+\gamma_+^Y}\right]=0$$

which, as above, can never be realised because all reaction rates must be equal or greater than zero. Therefore, we conclude that a simple negative feedback motif cannot explain the observed optimum in the dose-response curve.

We have also performed this analysis on a 3 node network with non-saturating mass action (Figure S 5d-f). As before, C_1 activates P which in this network indirectly activates the inhibitor X by the activation of Y. In this architecture we observe oscillations in time (Figure S5e) but a bell-shaped dose-response in the steady state was not possible (Figure S5f). In what follows we show that this model is a special case of the model presented above and in this way we show that it cannot produce bell-shaped dose-response curves.

The system of ODEs for this model is,

$$\frac{\mathrm{d}\hat{X}}{\mathrm{d}t} = \hat{\eta_+^Y}\hat{Y}(1-\hat{X})+\gamma_+^X(1-\hat{X})-\gamma_-^X\hat{X} \tag{8}$$

$$\frac{\mathrm{d}\hat{P}}{\mathrm{d}t} = (\lambda\hat{C_1}+\gamma_+^P)(1-\hat{P})-\gamma_-^P\hat{P}-\hat{\beta_-^X}\hat{X}\hat{P} \tag{9}$$

$$\frac{\mathrm{d}\hat{Y}}{\mathrm{d}t} = (\hat{\delta_+^P}\hat{P}+\gamma_+^Y)(1-\hat{Y})-\gamma_-^Y\hat{Y} \tag{10}$$

where $\hat{X}=\frac{X}{X_T}$, $\hat{P}=\frac{P}{P_T}$, $\hat{Y}=\frac{Y}{Y_T}$, $\hat{\eta_+^Y}=\eta_+^Y Y_T$, $\hat{\beta_-^X}=\beta_-^X X_T$ and $\hat{\delta_+^P}=\delta_+^P P_T$. In the steady-state we find,

$$\begin{aligned}\hat{X} &= \frac{(\lambda\hat{C_1}+\gamma_+^P)(\frac{1}{\hat{P}}-1)-\gamma_-^P}{\hat{\beta_-^X}}\\ \hat{Y} &= \frac{1}{1+\frac{\gamma_-^Y}{\hat{\delta_+^P}\hat{P}+\gamma_+^Y}}\end{aligned} \quad ,$$

which can be substituted into the steady-state expression for $\frac{\mathrm{d}\hat{X}}{\mathrm{d}t}$ to obtain an implicit equation for $\hat{P}$ in terms of the parameters of the system,

$$g = 1 - \left[1 + \frac{\gamma_-^X}{\frac{\eta_+^{\hat{Y}}}{1+\frac{\gamma_-^Y}{\delta_+^{\hat{P}}\hat{P}+\gamma_+^Y}} + \gamma_+^X}\right]\left[\frac{\kappa\left(\frac{1}{\hat{P}} - 1\right) - \gamma_-^P}{\beta_-^{\hat{X}}}\right] = 0 \tag{11}$$

where again, $\kappa = \lambda\hat{C}_1 + \gamma_+^P$. When $n = 1$ the equation for f (derived above) is identical to the equation of g with the exception of a constant. Given that the conclusions above are independent of n it follows that we can conclude that this 3 node network with negative feedback cannot exhibit bell-shaped dose-response curves in the steady-state. This is consistent with results from the systematic network analysis that did not find any negative feedback networks compatible with the phenotypic features.

Predicted T cell activation by co-presentation of pMHC ligands in the KPL-IFF model

The KPL-IFF model was extended to include an additional pMHC by first calculating the fraction of TCR bound to each ligand at steady-state using the following set of coupled ODEs,

$$\begin{aligned}
\mathrm{d}L^1/\mathrm{d}t &= -k_{\text{on}}^1 L^1 R + k_{\text{off}}^1 C^1 \\
\mathrm{d}L^2/\mathrm{d}t &= -k_{\text{on}}^2 L^2 R + k_{\text{off}}^2 C^2 \\
\mathrm{d}R/\mathrm{d}t &= -k_{\text{on}}^1 L^1 R + k_{\text{off}}^1 C^1 - k_{\text{on}}^2 L^2 R + k_{\text{off}}^2 C^2 \\
\mathrm{d}C^1/\mathrm{d}t &= k_{\text{on}}^1 L^1 R - k_{\text{off}}^1 C^1 \\
\mathrm{d}C^2/\mathrm{d}t &= k_{\text{on}}^2 L^2 R - k_{\text{off}}^2 C^2
\end{aligned}$$

where C^1 and C^2 are, respectively, the concentration of TCR bound to the first and second pMHC ligands. These ODEs were integrated to the steady-state to determine C^1 and C^2, which were used to calculate P as follows,

$$\begin{aligned}
\hat{C}_1^1 &= \left(\frac{k_{\text{off}}^1}{k_{\text{off}}^1 + k_{\text{p}}}\right)\left(\frac{k_{\text{p}}}{k_{\text{off}}^1 + \phi k_{\text{p}}}\right)\hat{C}^1 \\
\hat{C}_1^2 &= \left(\frac{k_{\text{off}}^2}{k_{\text{off}}^2 + k_{\text{p}}}\right)\left(\frac{k_{\text{p}}}{k_{\text{off}}^2 + \phi k_{\text{p}}}\right)\hat{C}^2 \\
\hat{Y} &= \frac{1 + \hat{\lambda}(\hat{C}_1^1 + \hat{C}_1^2)}{1 + \hat{\lambda}(\hat{C}_1^1 + \hat{C}_1^2) + \hat{\gamma}^y} \\
\hat{P} &= \frac{1 + \hat{\delta}\hat{Y}}{1 + \hat{\delta}\hat{Y} + \hat{\gamma}^p + \hat{\mu}(\hat{C}_1^1 + \hat{C}_1^2)}
\end{aligned}$$

where superscripts indicate ligand identity (1 or 2). Parameter values are identical to those used to generate Figure 3d with the ligand concentration and kinetic parameters as indicated in Figure 5.

Model of kinetic proofreading with limited signalling followed by TCR internalisation

The following ODEs were used to model kinetic proofreading with limited signalling with constitutive and induced TCR internalisation,

$$\begin{aligned}
\mathrm{d}L/\mathrm{d}t &= -k_{\mathrm{on}}LR + k_{\mathrm{off}}(C_0 + C_1 + C_2) + \beta(C_0 + C_1 + C_2) \\
\mathrm{d}R/\mathrm{d}t &= -k_{\mathrm{on}}LR + k_{\mathrm{off}}(C_0 + C_1) + \alpha - \beta R \\
\mathrm{d}C_0/\mathrm{d}t &= k_{\mathrm{on}}LR - (k_{\mathrm{off}} + k_{\mathrm{p}} + \beta)C_0 \\
\mathrm{d}C_1/\mathrm{d}t &= k_{\mathrm{p}}C_0 - (k_{\mathrm{off}} + \phi k_{\mathrm{p}} + \beta)C_1 \\
\mathrm{d}C_2/\mathrm{d}t &= \phi k_{\mathrm{p}}C_1 - (k_{\mathrm{off}} + \beta)C_2
\end{aligned}$$

where α and β are the constitutive receptor recycling rates. In this model, it is assumed that C_2 represents a state where the receptor is tagged for induced internalisation so that immediately upon pMHC unbinding it is internalised (i.e. $k_{\mathrm{off}}C_2$ does not appear in the equation for R). The model is integrated to the steady-state using the Matlab (Mathworks, MA) function *ode23s* with the parameters indicated in Figure S8.

Supplementary Movies

Movie S1. Systematic analysis of 304 network architectures (Figure 4a). Each 1 second frame shows the network architecture (left) and the network output (right). The network architecture displays the 3 receptor states (C_0, C_1, and C_2) together with Y and P where green arrows indicate activation and red arrows indicate inhibition (magnitudes of inhibition arrows are in italics). The network output displays P (y-axis) over the ligand concentration (x-axis) for ligands with decreasing k_{off} (blue to red). Networks appear in ascending order of the SSR with networks that are better able to produce the phenotypic features appearing first. See Supplementary Information for computational details.

Movie S2. Systematic analysis of 26,069 network architectures (Figure 4e). Movie generated as described (see Movie S1) except that one additional receptor state and one additional node were included (see main text and Figure 4e for details). This movie can be found at this link: https://dx.doi.org/10.6084/m9.figshare.3491792.v1

Supplementary Applet

Applet S1. A Javascript applet that can be used to examine how the 5 model parameters (k_{p}, ϕ, μ, λ, and δ) modulate the predicted dose-response for ligands of varying affinities for the KPL-IFF model (Figure 3d). Default parameter values in the applet are the same as those used to generate Fig. 3d. This applet can be found at this link: https://dx.doi.org/10.6084/m9.figshare.3491807.v1

Supplementary Table

pMHC	Peptide	k_{off} (s^{-1})	SEM	k_{on} ($M^{-1}s^{-1}$)	SEM	K_D (M)	SEM
9V	SLLMWITQV	8.26E-05	1.03E-06	1.17E+06	2.80E+04	7.07E-11	2.57E-12
4A	SLLAWITQV	1.54E-03	1.77E-05	1.41E+06	1.15E+05	1.09E-09	1.01E-10
5Y	SLLMYITQV	1.67E-03	1.18E-04	1.26E+06	3.14E+05	1.33E-09	4.26E-10
8S	SLLMWITSV	1.33E-02	2.29E-03	1.03E+06	2.72E+05	1.29E-08	5.64E-09
6T	SLLMWTTQV	7.14E-02	1.43E-02	8.64E+05	2.70E+05	8.27E-08	3.58E-08
5F	SLLMFITQV	1.01E-01	7.08E-03	1.09E+06	2.03E+05	9.31E-08	2.39E-08
8K	SLLMWITKV	8.33E-02	6.46E-03	4.10E+05	2.98E+04	2.03E-07	3.05E-08
5P	SLLMPITQV	9.80E-01	7.76E-02	2.02E+06	2.39E+05	4.85E-07	9.59E-08
4A8K	SLLAWITKV	1.95E+00	5.31E-02	1.10E+06	1.34E+05	1.78E-06	2.65E-07
4A5A	SLLAAITQV	5.64E+00	5.62E-01	2.52E+05	5.47E+04	2.24E-05	7.10E-06
4A5P8K	SLLAPITKV					>1.0E-04	

Table S 1: Measured binding properties for the c58c61 TCR for the indicated peptide in complex with HLA-A*02:01 (pMHC ligand). Results are averages of at least 3 measurements.

Supplementary Figures

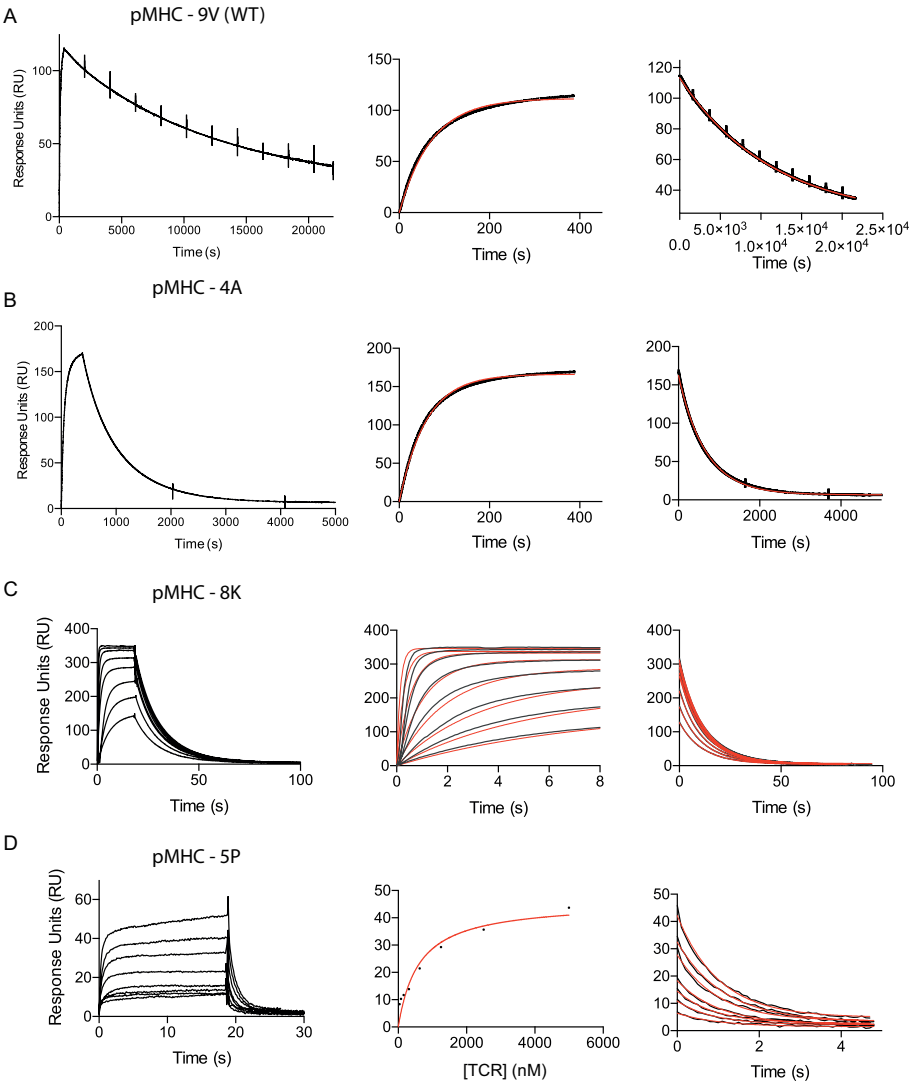

Figure S1: Representative surface plasmon resonance (SPR) measurements of TCR-pMHC interactions (Table S1). All experiments are performed by injecting recombinant c58c61 TCR over immobilised recombinant pMHC (see Materials & Methods). The precise protocol for determining the kinetic rate constants (k_{on} and k_{off}) was dependent upon the affinity regime of the TCR-pMHC interaction. a-b) In the case of TCR-pMHC interaction with small k_{off}, a single concentration of TCR is injected over the surface. The value of k_{off} is determined from the dissociation curve (right) which is used to fit the association curve (middle) with exponential rate of $k_{\text{on}}[\text{TCR}]+k_{\text{off}}$. c-d) In the case of TCR-pMHC interactions with a larger k_{off}, multiple concentrations of the TCR were injected over the surface. The value of k_{off} was determined from the dissociation curve and the value of k_{on} was either determined from fitting the association curves (as in c) or by first determining the K_{D} ($k_{\text{on}} = k_{\text{off}}/K_{\text{D}}$, as in d). When kinetics were too rapid to be resolved we only report the value of K_{D}. See Materials & Methods for a detailed protocol and mathematical analysis of the data.

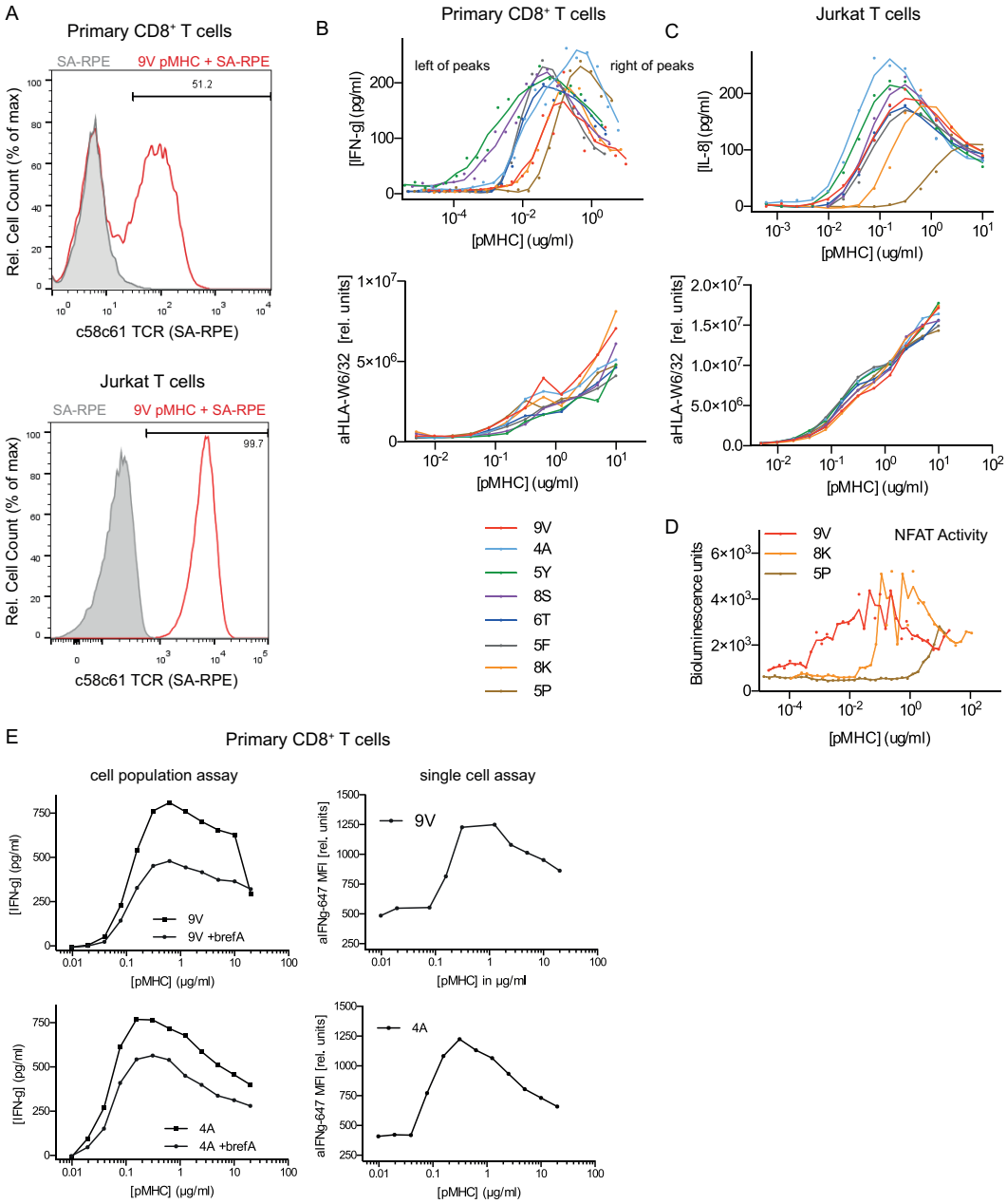

Figure S2: a) Expression of the c58c61 TCR on primary CD8$^+$ T cells and Jurkat T cells using the biotinylated high affinity pMHC (9V) with R-PE-conjugated streptavidin (red line) or only R-PE-conjugated streptavidin as a staining control (grey line). The Jurkat T cells were sorted following transduction. b,c) Functional assays (top) together with pMHC immobilisation controls (bottom) for b) primary CD8$^+$ T cells and c) Jurkat T cells with a larger number of higher affinity ligands. Functional assays were corrected for differences in pMHC immobilisation (see Materials & Methods). d) The transcriptional activity of NFAT in Jurkat T cells was determined at 16 hours for the indicated pMHC ligands revealing qualitatively similar behaviour to IL-8. This reporter of T cell activation was not used routinely because of the poor signal-to-noise ratio of the assay. e) Activation assays with primary T cells were performed as described in the main text for the indicated pMHC except that brefeldin A was added to block cytokine secretion for the last 2 hours of the assay (reducing the amount of supernatant cytokine in the cell population assay, left column) at which point intracellular cytokine levels were determined by flow cytometery (right column). The supernatant concentration of cytokine (cell population assay) compares favorably with the mean intensity of cytokine in the positive population (single cell assay). All data are representative of at least 3 independent experiments.

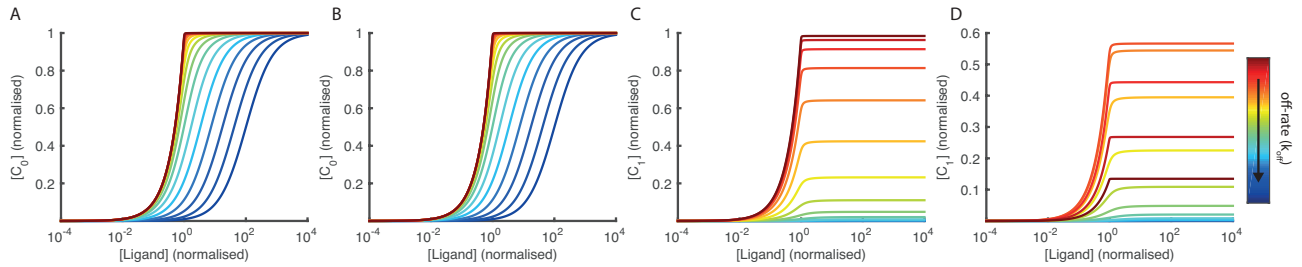

Figure S3: The concentration of TCR-pMHC complexes that regulate the activation of P for the phenotypic model calculations in Figure 3. The concentration of a) C_0 in the occupancy model, b) C_0 in the occupancy coupled to incoherent feedforward model, c) C_1 in the kinetic proofreading coupled to incoherent feedforward model, and d) C_1 in the KPL-IFF model. The maximum concentration of signalling competent TCR-pMHC complexes for the occupancy models (a,b) is independent of the TCR-pMHC off-rate (k_{off}) whereas for the kinetic proofreading models (c,d) the maximum concentration of signalling competent TCR-pMHC complexes is dependent on the off-rate.

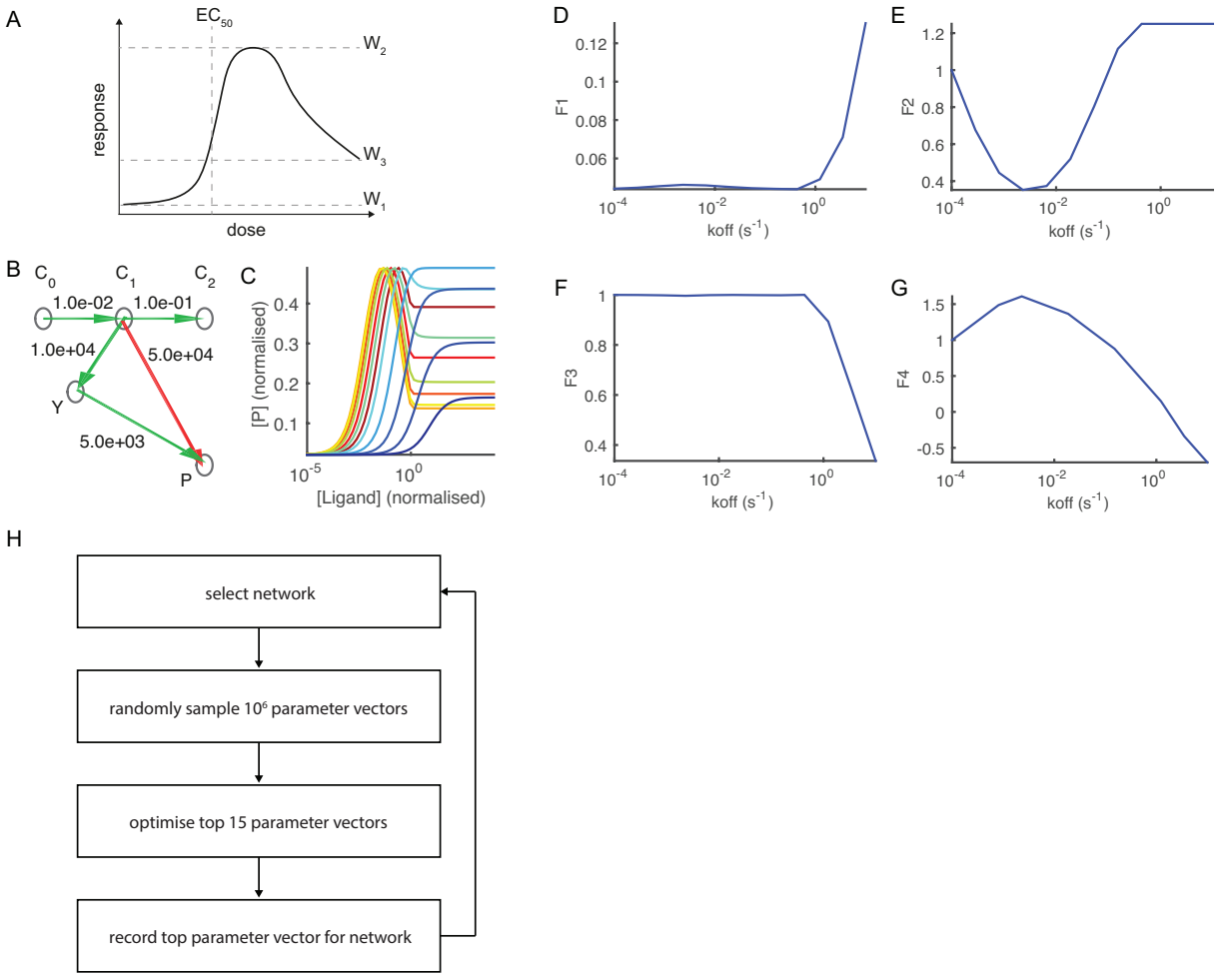

Figure S4: Quantitative metrics for comparing signalling network outputs. a) Schematic of a bell-shaped dose-response showing the definition of W_1, W_2, W_3, and EC_{50}. b) Schematic of the network architecture of the KPL-IFF phenotypic model where green arrows indicate activation and red arrows indicate inhibition with the magnitude of the arrow indicated (compare to Figure 3d). c) Output of the KPL-IFF phenotypic model shown in B with 12 pMHC ligands whose k_{off} varies from 10^{-4} (red) to 10 (blue). d-g) The values of the metrics F_1, F_2, F_3, and F_4 as a function of k_{off} for the output in panel c. h) Workflow of the systematic network search algorithm.

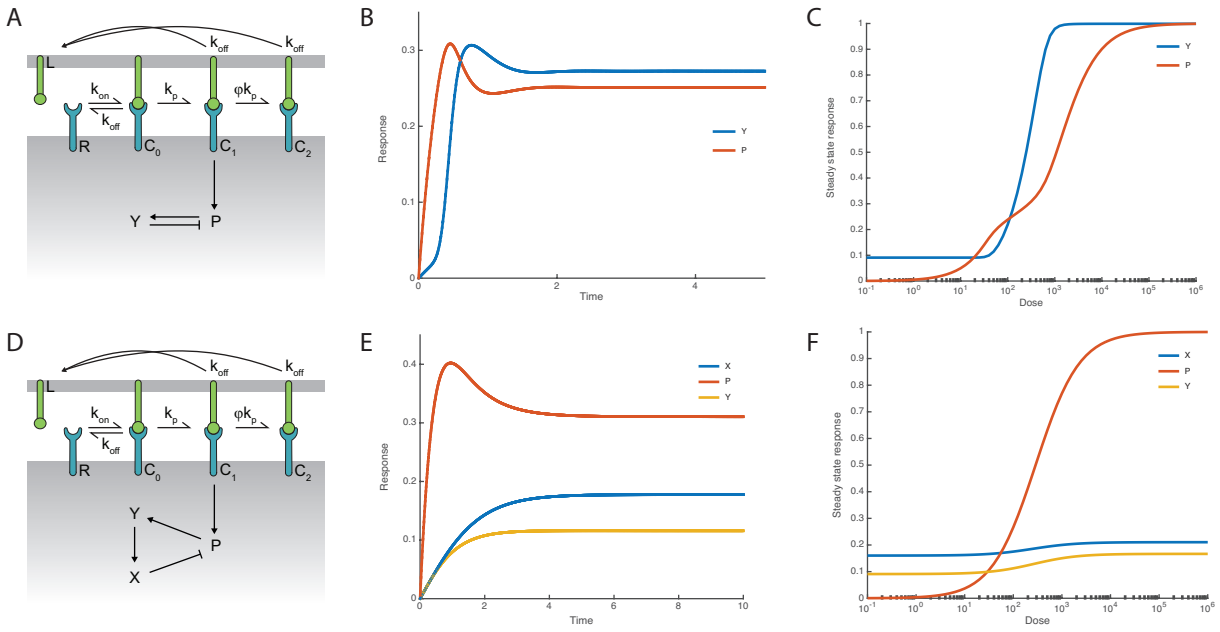

Figure S5: Negative feedback can produce oscillations in time but not bell-shaped dose-response curves in the steady-state. a) A two node negative feedback, whereby P activates its inhibitor Y (see Figure 4d) can b) produce oscillations in P over time but c) not bell-shaped dose-response in the steady-state. d) A three node negative feedback, where P activates Y which in turn activates X that is able to inhibit P can (as for the two component negative feedback) e) produce damped oscillations in P over time but f) not bell-shaped dose-response in the steady-state. See Supplementary Information for calculation details.

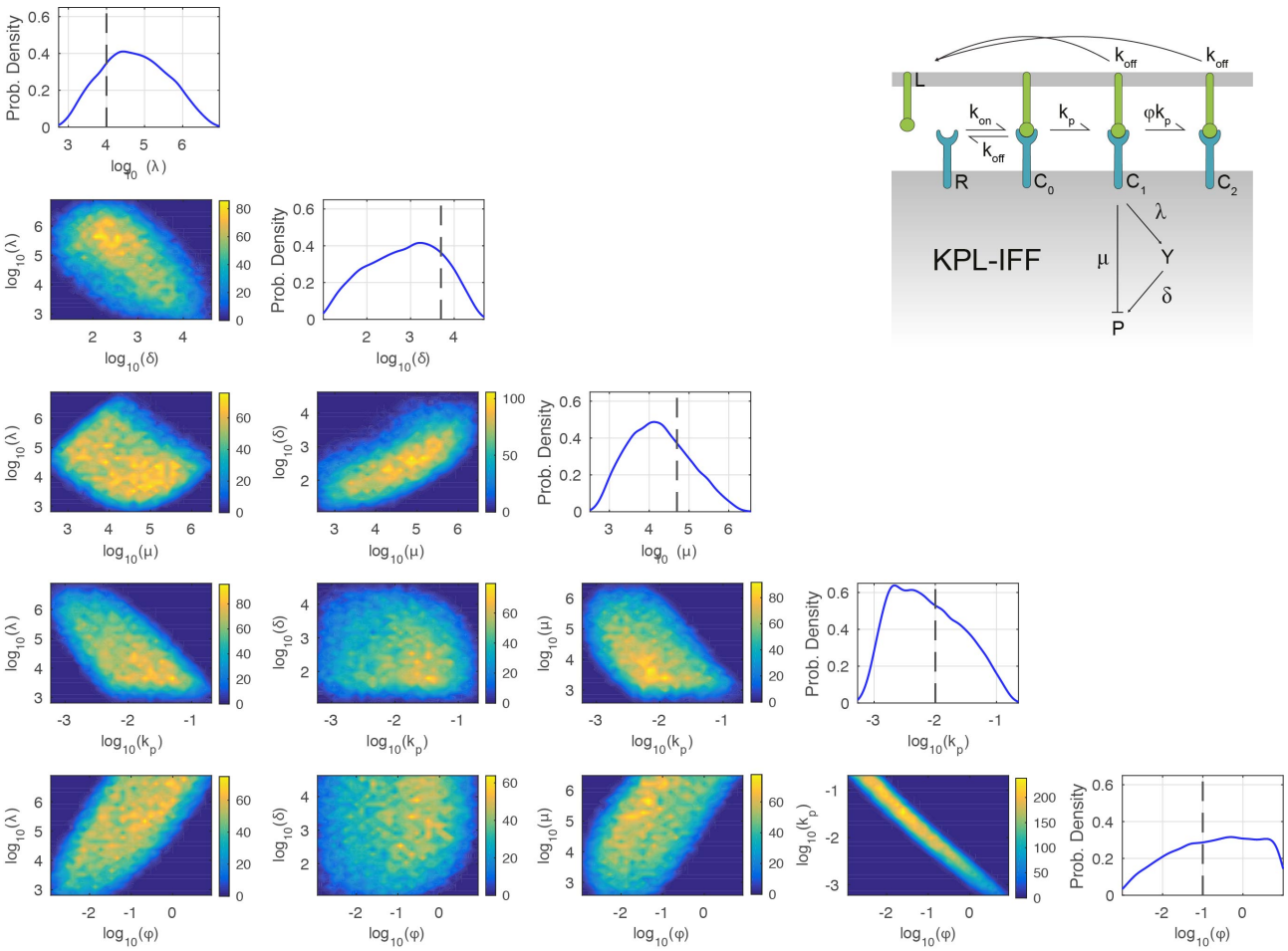

Figure S6: KPL-IFF model parameters compatible with phenotypic features. The probability density of the indicated parameter is shown along the diagonal along with pairwise correlations in the off-diagonals with yellow indicating a high frequency of occurence (scale bar indicates number of occurrences). Vertical dashed lines in the probability densities indicate the default parameter used in Figure 3d. We find a broad range of parameter values compatible with phenotypic features but with certain relationships amongst them. For example, we find that $\mu > \delta$ but both parameters can vary more than 1000-fold provided this relationship is maintained. See Supplementary Information for calculation details.

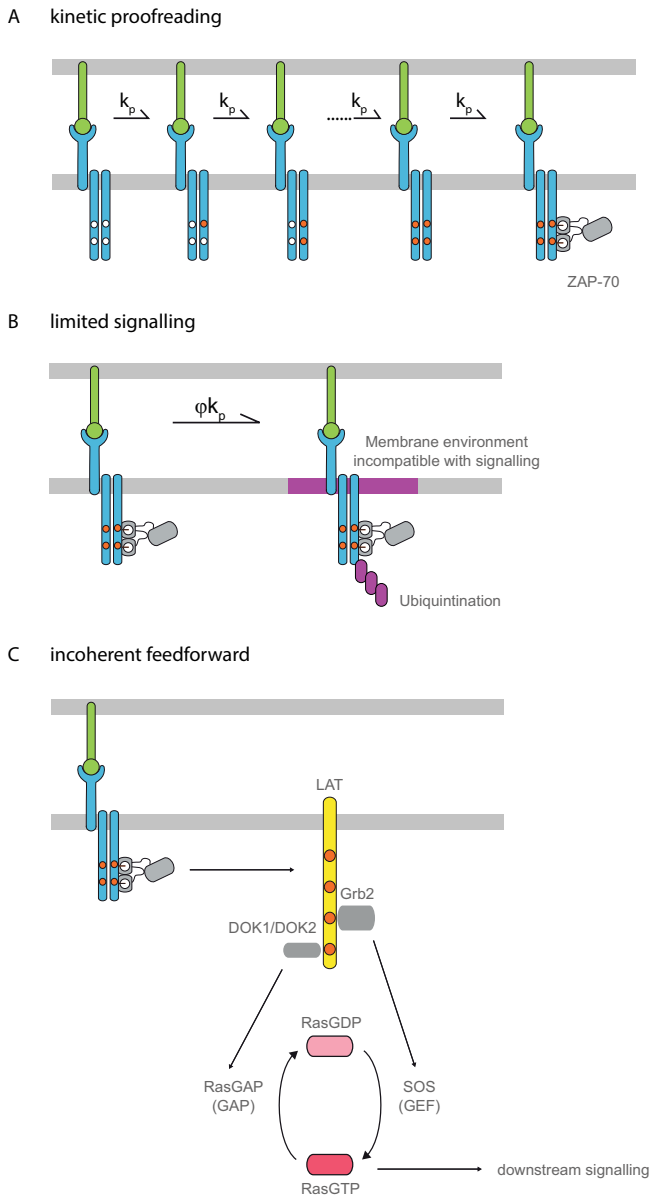

Figure S7: Possible relationships between the phenotypic model modules and known T cell signalling components. a) Kinetic proofreading can be realised by the sequential phosphorylation of the T cell receptor ITAMs and/or the recruitment of Lck associated coreceptors (5) (not shown) followed by the recruitment and subsequent activation of ZAP-70 (6) . b) Limited signalling of the T cell receptor may occur as a result of ubiquintination (7) and/or the receptor entering membrane environments that are incompatible with signalling (8). c) Incoherent feedforward in the signalling cascade initiated by the T cell receptor may occur between LAT and Ras (9). Phosphorylated LAT provides docking sites for Grb2 which recruits the guanine nucleotide exchange factor (GEF) SOS that promotes the formation of the active form of Ras (RasGTP) that promotes downstream signalling. However, phosphorylated LAT also provides docking sites for DOK1/DOK2 which recruits the GTPase activating protein (GAP) RasGAP that promotes the formation of RasGDP and hence reduces the active form of Ras. Although not depicted in the schematic, incoherent feedforward may also arise from the TCR signalosome because it is able to associate with both a tyrosine kinase (ZAP-70) and a tyrosine phosphatase (SHP-1) (10).

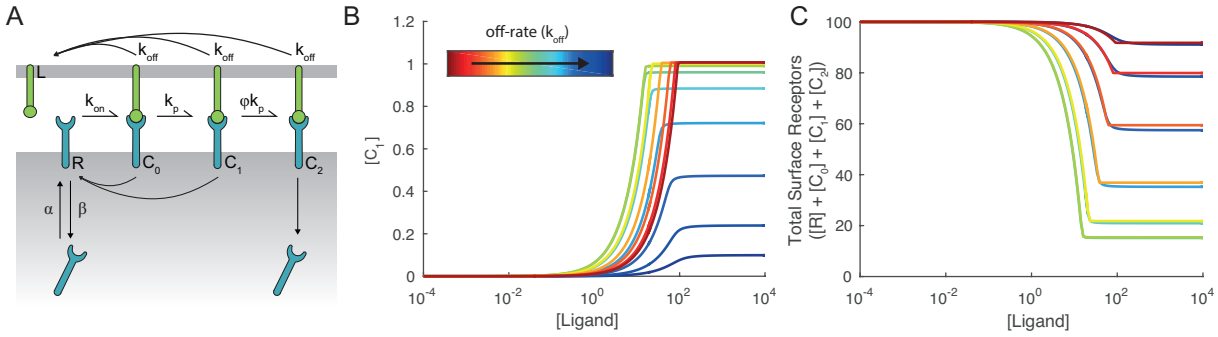

Figure S8: Internalisation of TCR following signalling does not produce bell-shaped dose-responses in the steady-state. a) Schematic of internalisation model that includes kinetic proofreading with limited signalling followed by TCR internalisation (from state C_2) with basal recycling of receptor at the cell surface. b) Concentration of signalling TCR and c) total surface TCR over ligand concentrations for different ligand affinities at steady-state. Parameters: $k_{\mathrm{p}} = 0.01\ \mathrm{s}^{-1}$, $\phi = 0.1$, $\alpha = 0.01\ \mu\mathrm{m}^{-2}\mathrm{s}^{-1}$, $\beta = 0.001\ \mathrm{s}^{-1}$ with a variation of k_{off} from 10^{-4} to 10^{2} s^{-1} (coloured lines).

References

1. Ma W, Trusina A, El-Samad H, Lim Wa, Tang C (2009) Defining network topologies that can achieve biochemical adaptation. *Cell* 138:760–73.

2. Shah Na, Sarkar Ca (2011) Robust network topologies for generating switch-like cellular responses. *PLoS Computational Biology* 7.

3. Toni T, Welch D, Strelkowa N, Ipsen a, Stumpf MP (2009) Approximate Bayesian computation scheme for parameter inference and model selection in dynamical systems. *Journal of The Royal Society Interface* 6:187–202.

4. Sunnåker M, et al. (2013) Approximate bayesian computation. *PLoS computational biology* 9:e1002803.

5. Stepanek O, et al. (2014) Coreceptor scanning by the T cell receptor provides a mechanism for T cell tolerance. *Cell* 159:333–345.

6. Acuto O, Di Bartolo V, Michel F (2008) Tailoring T-cell receptor signals by proximal negative feedback mechanisms. *Nature Reviews Immunology* 8:699–712.

7. Yang M, et al. (2015) K33-linked polyubiquitination of Zap70 by Nrdp1 controls CD8+ T cell activation. *Nature Immunology* 16:1–12.

8. Choudhuri K, et al. (2014) Polarized release of T-cell-receptor-enriched microvesicles at the immunological synapse. *Nature* 507:118–123.

9. Brownlie RJ, Zamoyska R (2013) T cell receptor signalling networks: branched, diversified and bounded. *Nature Reviews Immunology* 13:257–269.

10. Altan-Bonnet G, Germain RN (2005) Modeling T cell antigen discrimination based on feedback control of digital ERK responses. *PLoS biology* 3:e356.